

# Damped Bloch wave propagation in periodic architected viscoelastic materials: a Fourier-based scheme with quasi-Monte Carlo integration

Giacomo Elefante<sup>a</sup>, Francesca Fantoni<sup>\*b</sup>, Maria Laura De Bellis<sup>c</sup>, Andrea Bacigalupo<sup>\*d</sup>

<sup>a</sup>*IDSIA, USI Lugano, Lugano, Switzerland*

<sup>b</sup>*DICATAM, University of Brescia, Brescia, Italy*

<sup>c</sup>*INGEO, University of Chieti-Pescara, Pescara, Italy*

<sup>d</sup>*DICCA, University of Genova, Genova, Italy*

---

## Abstract

This paper investigates the behavior of microstructured viscoelastic metamaterials with complex topologies, focusing on their wave propagation characteristics, specifically the behavior of damped Bloch waves. Fourier-based methods are used to solve the governing dynamic equations, taking into account both spatial and temporal damping effects. The study addresses eigenproblems related to Bloch wave dispersion, with a particular emphasis on rational eigenproblems, which are solved using an enhanced derationalization technique previously proposed by the authors. To efficiently approximate the Fourier coefficients, the technique utilizes the quasi-Monte Carlo integration method, which is particularly effective for complex geometries. An illustrative example based on triply periodic minimal surface structures is provided to demonstrate the effectiveness of the proposed approach. The results highlight the potential of these metamaterials for applications in noise reduction, impact resistance, and other advanced engineering fields.

**Keywords:** Viscoelastic Metamaterials, Damped Bloch Waves, Fourier-based Methods, Quasi-Monte Carlo Integration, Derationalization Technique, Triply Periodic Minimal Surface (TPMS)

---

## 1. Introduction

Metamaterials with periodic complex topologies and viscoelastic phases are widely recognized for their capability to tailor mechanical properties and control wave propagation through optimized microstructural design and material composition [1–5]. These systems integrate the overall physical-mechanical response derived from complex topologies with the time-dependent behavior of viscoelastic phases. Such integration enables advanced functionalities, including controlled energy dissipation, selective wave filtering, vibration attenuation, shock mitigation, and mechanical energy trapping and absorption in response to impacts. The innovative design of these metamaterials, which may incorporate hierarchical microstructures, makes them suitable for applications such as noise-reduction devices, acoustic cloaks, and impact-resistant materials. Furthermore, their adaptability highlights potential applications in fields such as biomedical engineering, including prosthetic devices, tissue engineering scaffolds, and tunable structures for robotics and adaptive systems [6–15].

---

<sup>\*</sup>Corresponding authors. E-mail addresses: francesca.fantoni@unibs.it; andrea.bacigalupo@unige.it

Micromechanical models are utilized to rigorously characterize the behavior of individual phases and their interactions at the microscale, enabling a highly detailed description of the constitutive behavior of metamaterials. However, increased geometric complexity often renders these approaches computationally prohibitive due to the substantial resources required. In such instances, asymptotic, asymptotic variational and computational multiscale homogenization techniques offer more efficient and theoretically robust alternatives to direct micromechanical simulations. They enable the systematic derivation of effective macroscopic models—either local or non-local—that faithfully capture key microscale behaviors, even in the presence of complex multiphysics phenomena in periodic and/or quasi-periodic microstructures. These approaches ensure a consistent and predictive multiscale framework for representing the underlying mechanical and physical responses. [16–25]. To approximate the dispersive properties of metamaterials, particularly at high frequencies, advanced high-contrast and high-frequency asymptotic homogenization techniques are applied [26, 27]. For metamaterials with discrete microstructures, such as lattice or layered systems, continualization methods are also effective [28, 29]. Alternatively, the frequency band structure of a periodic metamaterial can be determined by solving the micromechanical problem using Floquet-Bloch theory, which involves an eigenproblem [30–32]. For complex topologies, advanced and efficient numerical methods are typically required for this solution [33].

In the case of metamaterials with viscoelastic phases, which are characterized by integro-differential field equations, the study of wave propagation can be approached either through integral transforms [2, 34, 35] or, alternatively, by employing added-variable approaches. In particular, the latter method allows the integro-differential problem—with a kernel expressed as a Dirichlet-Prony series—to be transformed into a higher-dimensional differential problem [36, 37]. For these viscoelastic metamaterials, the free propagation of Bloch waves in arbitrary directions is analyzed based on wave number and frequency. For Bloch waves with spatial damping, the waves are described by a generally complex wave number, and the problem is expressed as a polynomial algebraic eigenproblem parametrized by real frequency. Conversely, Bloch waves with temporal damping are characterized by a generally complex frequency, and the corresponding problem is formulated as a rational eigenproblem parametrized by real wave number. Rational eigenproblems, which are commonly encountered in the analysis of wave propagation in viscoelastic metamaterials, present significant challenges regardless of whether an analytical or computational approach is used. A potential solution to overcome these difficulties involves the use of derationalization techniques. More precisely, for a rational eigenproblem that includes both a polynomial and a rational component, where the rational term is the sum of scalar rational functions multiplied by constant matrices, a common method for solving it is to linearize the rational part, as outlined by Mehrmann and Voss in [38]. Linearization, in this case, transforms the problem by multiplying it by the scalar functions, which results in a polynomial eigenproblem of a higher degree. This new polynomial can then be solved using linearization techniques, such as those described by Mackey et al. in [39, 40] and others. However, this technique tends to be effective only for problems of low dimensionality. As an alternative, the rational eigenproblem can be approached as a general nonlinear eigenproblem, which can be tackled with nonlinear eigensolvers,

such as those proposed by Ruhe in [41] or more recently by Lietaert et al. in [42]. However, this method only provides approximate solutions and requires careful convergence analysis to verify its accuracy and effectiveness. An enhanced derationalization technique was proposed in [43], inspired by the work of Su and Bai in [44], and has demonstrated significant efficiency even for large-scale problems. More specifically, this technique proved instrumental in the design of a microstructured active metafilter with extruded planar geometry and a piezoelectric phase shunted to an RLC circuit. Within this framework, the present work investigates a microstructured viscoelastic metamaterial with arbitrary complex three-dimensional topologies. The objective is to develop a high-performance metafilter, studying both spatial and temporal damping associated with Bloch waves propagating through the periodic microstructure. The idea is to exploit the periodicity of the metamaterial by using a Fourier-based method to address the governing equations of the dynamic problem [45, 46]. Specifically, all periodic fields, both known and unknown, are expanded in Fourier series. In the case of simple geometries, as addressed in [43], it was possible to analytically determine the Fourier coefficients of the periodic constitutive tensors and inertial terms. However, when dealing with microstructures that have generic, complex topologies, as presented here, numerical approximations for these coefficients are generally required. The study of the free propagation of Bloch waves is characterized by an infinite-dimensional eigenproblem in terms of frequency and wave number, which is polynomial for spatial damping or rational for temporal damping. The problem is then truncated, and in the case of temporal damping, the enhanced derationalization technique is applied, based on LU factorization of the matrix containing the rational part of the eigenvalue problem, followed by linearization. This approach proves effective in computing the complex frequency Floquet–Bloch spectra ensuring good convergence. To reduce the computational burden in the numerical approximation of the Fourier coefficients, advanced techniques based on Monte Carlo (MC) or quasi-Monte Carlo (qMC) integration are often required. This is due to the need to handle the dense matrices of the coefficients involved in the eigenproblems addressed by the Fourier-based method.

MC and qMC methods are effective techniques for performing integration over complex domains [47–51]. The MC method relies on generating random samples from a probability distribution, while qMC uses deterministic samples, to estimate numerical quantities—in this case, integrals—by averaging the results of these samples. In particular, such methods approximate the integral of a function as

$$\int_{\Omega} f(\mathbf{x}) d\mathbf{x} \approx \frac{|\Omega|}{N} \sum_{i=1}^N f(\mathbf{x}_i),$$

where  $|\Omega|$  is the measure of the integration domain  $\Omega$  and  $N$  is the number of samples. Therefore, MC and qMC methods are cubature formulas with uniform positive weights, relying solely on a well-distributed set of points within the integration domain. These methods do not require prior knowledge of the domain’s geometry, making them particularly suitable for complex or irregular integration domains. For domains  $\Omega$  with complex geometries, a box  $\mathcal{B}$  containing  $\Omega$  is introduced, along with a set  $\mathcal{X}_M$  of  $M$  points well distributed within  $\mathcal{B}$ , which, for boxes, are well-known in literature. Using

the indicator (or characteristic) function of  $\Omega$  named  $\chi_\Omega(\mathbf{x})$ , the integral becomes:

$$\int_{\Omega} f(\mathbf{x}) d\mathbf{x} = \int_{\mathcal{B}} f(\mathbf{x}) \chi_\Omega(\mathbf{x}) d\mathbf{x} \approx \frac{|\mathcal{B}|}{M} \sum_{\substack{i=1 \\ \mathbf{x}_i \in \Omega}}^M f(\mathbf{x}_i).$$

In this way, it is possible to integrate over domains with complex geometries by relying solely on an indicator function for the domain, without requiring detailed knowledge of the geometry itself [52–54]. An important advantage of using MC and qMC methods for integration, as opposed to traditional tensor product cubature methods, is their ability to overcome the so-called curse of dimensionality. This refers to the exponential growth in the number of points required to maintain the same level of accuracy as the dimensionality increases. Unlike tensor product methods, which suffer from this exponential increase, MC and qMC methods exhibit convergence rates that are independent of the dimensionality. Specifically, the convergence rate for MC is of order  $O(N^{-1/2})$ , while for qMC it is of order  $O(N^{-1})$ . In light of the above considerations, this work focuses on qMC methods.

The structure of this paper is as follows. Section 2 provides an overview of the periodic architected material, focusing on its constitutive and governing equations in the dynamic regime. In Section 3, the propagation of damped Bloch waves is examined, focusing on temporal damping characterized by complex angular frequency and spatial damping described by complex wave number. Section 4 addresses the truncation of the infinite-dimensional eigenvalue problem and introduces a derationalization procedure for handling the resulting finite-dimensional rational eigenproblem. Section 5 presents the qMC integration scheme used to approximate the Fourier coefficients efficiently. An illustrative example of a viscoelastic architected material based on a triply periodic minimal surface (TPMS) structure is given in Section 6 to demonstrate the capabilities of the proposed approach. Finally, Section 7 concludes the paper with a summary of the main findings and suggestions for future research directions.

## 2. Constitutive characterization and field equations of the periodic architected material

One considers a periodic heterogeneous periodic architected material with a complex microstructural topology made of different phases distinguished between elastic and viscoelastic. The three-dimensional architected material is obtained through the spatial repetition of a periodic cell  $\mathfrak{A} = [0, \varepsilon] \times [0, \delta\varepsilon] \times [0, \zeta\varepsilon]$  along three perpendicular directions. In a Cartesian coordinate system  $\{\mathbf{e}_1, \mathbf{e}_2, \mathbf{e}_3\}$ , the periodic cell  $\mathfrak{A}$  is thus characterized by the three periodicity vectors  $\mathbf{v}_1 = \delta\mathbf{e}_1$ ,  $\mathbf{v}_2 = \delta\delta\mathbf{e}_2$ , and  $\mathbf{v}_3 = \zeta\delta\mathbf{e}_3$ . Denoting with  $\mathbf{x} = x_i\mathbf{e}_i$ , with  $i = 1, 2, 3$ , the position vector of each material point and  $t$  the time variable, the constitutive response of the different phases is described through the elastic relaxation tensor  $\mathbb{G}(\mathbf{x}, t) = G_{ijhk}(\mathbf{x}, t)\mathbf{e}_i \otimes \mathbf{e}_j \otimes \mathbf{e}_h \otimes \mathbf{e}_k$ , whose components are expressed in terms of a Prony series as

$$G_{ijhk}(\mathbf{x}, t) = G_{ijhk}^{(\infty)}(\mathbf{x}) \left[ 1 + \sum_{n=1}^N \gamma^n \exp\left(-\frac{t}{\tau_r^n(\mathbf{x})}\right) \right], \quad (1)$$



where  $G_{ijhk}^{(\infty)}(\mathbf{x})$  refers to the long-term response of the material,  $\gamma^n$  is the  $n$ -th viscosity ratio of the relaxation function and  $\tau_r^n$  represents the  $n$ -th relaxation time. The constitutive equation expressed in terms of a hereditary integral links the stress tensor  $\boldsymbol{\sigma}(\mathbf{x}, t) = \sigma_{ij}(\mathbf{x}, t)\mathbf{e}_i \otimes \mathbf{e}_j$  to the time derivative of the strain tensor  $\boldsymbol{\varepsilon}(\mathbf{x}, t) = \varepsilon_{ij}(\mathbf{x}, t)\mathbf{e}_i \otimes \mathbf{e}_j$  through (1) and it is expressed componentwise as

$$\sigma_{ij}(\mathbf{x}, t) = \int_{-\infty}^t G_{ijhk}(\mathbf{x}, t - \tau) \dot{\varepsilon}_{hk}(\mathbf{x}, \tau) d\tau. \quad (2)$$

Since  $\boldsymbol{\varepsilon} = \text{sym}(\nabla \mathbf{u})$ , with  $\mathbf{u}(\mathbf{x}, t) = u_i(\mathbf{x}, t)\mathbf{e}_i$  the displacement field vector, the substitution of (2) into the balance equation

$$\frac{\partial \sigma_{ij}(\mathbf{x}, t)}{\partial x_j} + b_i(\mathbf{x}, t) = \rho(\mathbf{x}) \ddot{u}_i(\mathbf{x}, t), \quad (3)$$

where  $b_i(\mathbf{x}, t)$  are the components of the body force vector  $\mathbf{b}(\mathbf{x}, t)$  and  $\rho(\mathbf{x})$  is the mass density, leads to the integrodifferential field equation governing the material behavior in the time domain, namely

$$\frac{\partial}{\partial x_j} \left( \int_{-\infty}^t G_{ijhk}(\mathbf{x}, t - \tau) \frac{\partial \dot{u}_h(\mathbf{x}, \tau)}{\partial x_k} d\tau \right) + b_i(\mathbf{x}, \tau) = \rho(\mathbf{x}) \ddot{u}_i(\mathbf{x}, t). \quad (4)$$

Exploiting the bilateral Laplace transform in time of an arbitrary, time-dependent real-valued function  $f(t)$ , defined as

$$\mathcal{L}(f(t)) = \hat{f}(s) = \int_{\mathbb{R}} f(t) \exp(-st) dt, \quad (5)$$

where  $s \in \mathbb{C}$  is the Laplace argument and  $\hat{f} : \mathbb{C} \rightarrow \mathbb{C}$ , the components of the relaxation tensor in the transformed space read

$$\hat{G}_{ijhk}(\mathbf{x}, s) = G_{ijhk}^{(\infty)}(\mathbf{x}) \left[ \frac{1}{s} + \sum_{n=1}^N \frac{\gamma^n \tau_r^n(\mathbf{x})}{s \tau_r^n(\mathbf{x}) + 1} \right]. \quad (6)$$

Since  $\mathcal{L}(\partial^n f(t)/\partial t^n) = s^n \mathcal{L}(f(t))$  and  $\mathcal{L}(f_1(t) * f_2(t)) = \mathcal{L}(f_1(t)) \mathcal{L}(f_2(t))$ , each phase is governed by the following equilibrium equation in the transformed space

$$\frac{\partial}{\partial x_j} \left( \hat{C}_{ijhk}(\mathbf{x}, s) \frac{\partial \hat{u}_h(\mathbf{x}, s)}{\partial x_k} \right) + \hat{b}_i(\mathbf{x}, s) = \rho(\mathbf{x}) s^2 \hat{u}_i(\mathbf{x}, s), \quad (7)$$

where  $\hat{b}_i(\mathbf{x}, s)$  are the components of the transformed body force vector and  $\hat{C}_{ijhk}(\mathbf{x}, s)$  are the components of the transformed elastic tensor  $\hat{\mathbb{C}} = \hat{C}_{ijhk} \mathbf{e}_i \otimes \mathbf{e}_j \otimes \mathbf{e}_h \otimes \mathbf{e}_k$ . For a linear viscoelastic phase they can be related to the components of the transformed relaxation tensor through the relation  $\hat{C}_{ijhk}(s) = s \hat{G}_{ijhk}(s)$ , while if the phase is linear elastic they results to be  $s$ -independent and simply denoted as  $C_{ijhk}$ . Because of the periodicity of the architected material, the constitutive and inertial properties are such that

$$\hat{C}_{ijhk}(\mathbf{x} + z\mathbf{v}_l, s) = \hat{C}_{ijhk}(\mathbf{x}, s), \quad \rho(\mathbf{x} + z\mathbf{v}_l) = \rho(\mathbf{x}), \quad \forall \mathbf{x} \in \mathfrak{U}, \quad l = 1, 2, 3, \quad z \in \mathbb{Z}. \quad (8)$$

As an alternative to the Prony series to characterize the viscoelastic kernel, further constitutive mod-

els have been proposed in the literature to describe the complex relaxation behavior of viscoelastic materials, including approaches based on fractional calculus, which are particularly effective in capturing memory effects and temperature-dependent phenomena, as in the case of thermo-rheologically complex polymers [55–57].

### 3. Damped Bloch wave propagation and complex frequency band structure

In order to investigate the propagation of damped Bloch waves inside an architected material having a complex microstructure, due to the Floquet-Bloch theory,  $\hat{u}_i$  can be decomposed as

$$\hat{u}_i = \tilde{u}_i e^{-i(\mathbf{k} \cdot \mathbf{x})}, \quad (9)$$

where  $\tilde{u}_i$  are the  $\mathfrak{A}$ -periodic Bloch amplitude components. They are such that

$$\tilde{u}_i(\mathbf{x} + z\mathbf{v}_l, \mathbf{k}, s) = \tilde{u}_i(\mathbf{x}, \mathbf{k}, s), \quad \forall \mathbf{x} \in \mathfrak{A}, l = 1, 2, 3, z \in \mathbb{Z} \quad (10)$$

where  $\mathbf{k} = k_j \mathbf{e}_j, j = 1, 2, 3$ , is the wave vector, spanning all points of the reciprocal space, also known as  $\mathbf{k}$ -space. The elementary periodic cell in such space is known as the first Brillouin zone and is denoted as  $\mathcal{B}$ . Due to the periodicity we can uniquely identify the periodic reciprocal lattice as the discrete subgroup  $\mathcal{G} := \{\mathbf{G} : \mathbf{G} = m_i \mathbf{p}_i; m_i \in \mathbb{Z}, i = 1, 2, 3\} \in \mathbb{R}^3$ , being  $\mathbf{p}_i = p_j^i \mathbf{e}_j, j = 1, 2, 3$ . The periodicity vectors of the reciprocal lattice  $\mathbf{p}_i$  are defined as

$$\mathbf{p}_1 = \frac{2\pi}{V} \mathbf{v}_2 \times \mathbf{v}_3, \quad \mathbf{p}_2 = \frac{2\pi}{V} \mathbf{v}_3 \times \mathbf{v}_1, \quad \mathbf{p}_3 = \frac{2\pi}{V} \mathbf{v}_1 \times \mathbf{v}_2, \quad (11)$$

where  $V = \mathbf{v}_1 \cdot (\mathbf{v}_2 \times \mathbf{v}_3)$  is the scalar triple product and corresponds to the volume of the cuboid defined by the three vectors  $\mathbf{v}_i$ , in order to have that the dot product  $\mathbf{v}_r \cdot \mathbf{p}_s = 2\pi\delta_{rs}$  holds. Inserting equation (9) in (7) leads to

$$\frac{\partial}{\partial x_j} \left( \hat{C}_{ijh\ell} \frac{\partial \tilde{u}_h}{\partial x_\ell} \right) - \iota k_\ell \left( \left( \hat{C}_{ijh\ell} + \hat{C}_{i\ell h j} \right) \frac{\partial \tilde{u}_h}{\partial x_j} + \frac{\partial \hat{C}_{ijh\ell}}{\partial x_j} \tilde{u}_h \right) - (k_j k_\ell \hat{C}_{ijh\ell} + \rho s^2 \delta_{ih}) \tilde{u}_h = 0. \quad (12)$$

Because of the  $\mathfrak{A}$ -periodicity of the constitutive tensor components  $\hat{C}_{ijh\ell}$ , of the mass density  $\rho$  and of the Bloch amplitude components  $\tilde{u}_i$ , their expansion in Fourier series with respect to the lattice  $\mathbf{G}$  can be defined as

$$\tilde{u}_i = \sum_{\mathbf{n} \in \mathbb{Z}^3} [\tilde{u}_i]_{\mathbf{n}} e^{i\mathbf{G}(\mathbf{n}) \cdot \mathbf{x}}, \quad [\tilde{u}_i]_{\mathbf{n}} = \frac{1}{|\mathfrak{A}|} \int_{\mathfrak{A}} \tilde{u}_i e^{-i\mathbf{G}(\mathbf{n}) \cdot \mathbf{x}} d\mathbf{x}, \quad (13a)$$

$$\rho = \sum_{\mathbf{v} \in \mathbb{Z}^3} [\rho]_{\mathbf{v}} e^{i\mathbf{G}(\mathbf{v}) \cdot \mathbf{x}}, \quad [\rho]_{\mathbf{v}} = \frac{1}{|\mathfrak{A}|} \int_{\mathfrak{A}} \rho e^{-i\mathbf{G}(\mathbf{v}) \cdot \mathbf{x}} d\mathbf{x}, \quad (13b)$$

$$\hat{C}_{ijh\ell} = \sum_{\mathbf{v} \in \mathbb{Z}^3} [\hat{C}_{ijh\ell}]_{\mathbf{v}} e^{i\mathbf{G}(\mathbf{v}) \cdot \mathbf{x}}, \quad [\hat{C}_{ijh\ell}]_{\mathbf{v}} = \frac{1}{|\mathfrak{A}|} \int_{\mathfrak{A}} \hat{C}_{ijh\ell} e^{-i\mathbf{G}(\mathbf{v}) \cdot \mathbf{x}} d\mathbf{x}, \quad (13c)$$

where  $\mathbf{n} = (n_1, n_2, n_3)$ ,  $\mathbf{v} = (v_1, v_2, v_3)$  with  $\mathbf{n}, \mathbf{v} \in \mathbb{Z}^3$ , and  $|\mathfrak{A}|$  is the size of the periodic cell. Then, the derivatives appearing in (12) read

$$\frac{\partial \tilde{u}_i}{\partial x_j} = \sum_{\mathbf{n} \in \mathbb{Z}^3} \iota(n_r p_j^r) [\tilde{u}_i]_{\mathbf{n}} e^{i\mathbf{G}(\mathbf{n}) \cdot \mathbf{x}}, \quad (14a)$$

$$\frac{\partial^2 \tilde{u}_i}{\partial x_\ell \partial x_j} = - \sum_{\mathbf{n} \in \mathbb{Z}^3} (n_r p_j^r)(n_s p_\ell^s) [\tilde{u}_i]_{\mathbf{n}} e^{i\mathbf{G}(\mathbf{n}) \cdot \mathbf{x}}, \quad (14b)$$

$$\frac{\partial \hat{C}_{ijh\ell}}{\partial x_j} = \sum_{\mathbf{v} \in \mathbb{Z}^3} \iota(v_r p_j^r) [\hat{C}_{ijh\ell}]_{\mathbf{v}} e^{i\mathbf{G}(\mathbf{v}) \cdot \mathbf{x}}. \quad (14c)$$

Hence, inserting the Fourier expansions (13) and (14) into equation (12), the following equation can be obtained

$$\begin{aligned} \sum_{\mathbf{n} \in \mathbb{Z}^3} \sum_{\mathbf{v} \in \mathbb{Z}^3} \Big( & - (v_r p_j^r)(n_s p_\ell^s) [\hat{C}_{ijh\ell}]_{\mathbf{v}} [\tilde{u}_h]_{\mathbf{n}} - (n_r p_j^r)(n_s p_\ell^s) [\hat{C}_{ijh\ell}]_{\mathbf{v}} [\tilde{u}_h]_{\mathbf{n}} + (n_r p_j^r) k_\ell [\hat{C}_{ijh\ell}]_{\mathbf{v}} [\tilde{u}_h]_{\mathbf{n}} \\ & + (n_r p_j^r) k_\ell [\hat{C}_{ih\ell}]_{\mathbf{v}} [\tilde{u}_h]_{\mathbf{n}} + (v_r p_j^r) k_\ell [\hat{C}_{ijh\ell}]_{\mathbf{v}} [\tilde{u}_h]_{\mathbf{n}} - k_j k_\ell [\hat{C}_{ijh\ell}]_{\mathbf{v}} [\tilde{u}_h]_{\mathbf{n}} - [\rho]_{\mathbf{v}} s^2 \delta_{ih} [\tilde{u}_h]_{\mathbf{n}} \Big) e^{i(\mathbf{G}(\mathbf{n}) + \mathbf{G}(\mathbf{v})) \cdot \mathbf{x}} = 0. \end{aligned} \quad (15)$$

Notice that in general the terms  $\hat{C}_{ijh\ell}$ , as well as  $\rho$ , are piece-wise constant functions, characterizing the different phases of the architected material. In order to investigate the propagation of damped Bloch waves inside the periodic material, an algebraic eigenproblem needs to be characterized, whose solution describes the wave dispersion features. In the most general case, both the wave vector  $\mathbf{k}$  and the angular frequency  $s$  are complex-valued, namely  $\mathbf{k} = (k_{1r} + i k_{1i}) \mathbf{e}_1 + (k_{2r} + i k_{2i}) \mathbf{e}_2 + (k_{3r} + i k_{3i}) \mathbf{e}_3$  and  $s = s_r + i s_i$ , and the wave is said to be spatially and temporally damped. The wave vector can also be written as  $\mathbf{k} = \mathbf{k}_r + i \mathbf{k}_i = k_r \mathbf{n}_r + i k_i \mathbf{n}_i$ , separating the contribution of the real wave vector  $\mathbf{k}_r$  having magnitude  $k_r$  and direction  $\mathbf{n}_r \in \mathbb{R}^3$ , which characterizes the wave propagation, and the contribution of the imaginary wave vector  $\mathbf{k}_i$ , with magnitude  $k_i$  and direction  $\mathbf{n}_i \in \mathbb{R}^3$ , which describes the wave spatial attenuation. If  $\mathbf{n}_r \neq \mathbf{n}_i$  the wave is denoted as non homogeneous, otherwise, when the directions of propagation and attenuation coincide, the wave is called homogeneous and  $\mathbf{k} = (k_r + i k_i) \mathbf{n} = k \mathbf{n}$ , with  $k$  the complex wave number.

In the case of homogeneous Bloch waves with temporal damping only, the wave vector is assumed to be real-valued and the Laplace variable  $s$ , representing the complex angular frequency, plays the role of the eigenvalue in the above-mentioned eigen-problem. In particular, a rational algebraic eigenproblem arises, whose solution is generally obtained by adopting suitable derationalization procedures. In this regard, one improved derationalization procedure is proposed in Section 4. The dispersion curves are thus expressed in terms of a complex frequency parameterized by the real wave vector and allow the investigation of temporal damping which is caused, in this case, by the viscous dissipation inside the material. If the spatial damping needs to be investigated, instead, which can be caused by spatial attenuation phenomena due to the presence of a periodic microstructure, Bragg or Mie refraction, and by viscous dissipation mechanisms, is the complex wave vector  $\mathbf{k}$  that plays the role of the eigenvalue of the algebraic eigenproblem. In particular, once  $\mathbf{n}_r$  and  $\mathbf{n}_i$  are fixed, as well as the complex

frequency, dispersion properties are investigated through the resolution of an algebraic eigenproblem polynomial in the wave number  $k$ . If then the frequency  $s = i\omega$  with  $\omega \in \mathbb{R}$ , dispersion curves are expressed in terms of the complex  $k$  parameterized by  $\omega$ . In the following, temporal and spatial damping are separately investigated considering the propagation of a homogeneous Bloch wave inside the periodic material.

### 3.1. Temporal damping: complex angular frequency parameterized by the wave number

Following the first of the two strategies, where  $s$  is complex and plays the role of the eigenvalue while  $\mathbf{k}$  is a real-valued parameter, allows investigating the temporal damping for the material at hand. The  $s$ -dependent coefficients of the Fourier series of the viscoelastic phases and those  $s$ -independent of the elastic phases can be split, due to the linearity of the integral computing the Fourier coefficient, and be denoted by  $[C_{ijh\ell}^{\mathfrak{C}}]_{\mathbf{n}}$  and  $[C_{ijh\ell}^{\mathfrak{A} \setminus \mathfrak{C}}]_{\mathbf{n}}$ , respectively. In this setting,  $\mathfrak{C}$  denotes the region of the periodic cell related to the viscoelastic phases, which are  $s$ -dependent, and  $\mathfrak{A} \setminus \mathfrak{C}$  the remaining region related to elastic phases, which are  $s$ -independent. It follows that the Fourier coefficients of  $\hat{C}_{ijh\ell}$  become

$$[\hat{C}_{ijh\ell}]_{\mathbf{n}} = [C_{ijh\ell}^{\mathfrak{A} \setminus \mathfrak{C}}]_{\mathbf{n}} + [C_{ijh\ell}^{\mathfrak{C}}]_{\mathbf{n}} = [C_{ijh\ell}^{\mathfrak{A} \setminus \mathfrak{C}}]_{\mathbf{n}} + r_{ijh\ell}(s)[\chi_{\mathfrak{C}}]_{\mathbf{n}}, \quad (16)$$

where  $r_{ijh\ell}$  denotes a generic rational polynomial function in  $s$  and  $\chi_{\mathfrak{C}}$  is the indicator function related to the set (region)  $\mathfrak{C}$ . Inserting equation (16) in equations (15) one has

$$\begin{aligned} \sum_{\mathbf{n} \in \mathbb{Z}^3} \sum_{\mathbf{v} \in \mathbb{Z}^3} & \left( - (v_r p_j^r)(n_s p_\ell^s) [C_{ijh\ell}^{\mathfrak{A} \setminus \mathfrak{C}}]_{\mathbf{v}} [\tilde{u}_h]_{\mathbf{n}} - (n_r p_j^r)(n_s p_\ell^s) [C_{ijh\ell}^{\mathfrak{A} \setminus \mathfrak{C}}]_{\mathbf{v}} [\tilde{u}_h]_{\mathbf{n}} + (n_r p_j^r) k_\ell [C_{ijh\ell}^{\mathfrak{A} \setminus \mathfrak{C}}]_{\mathbf{v}} [\tilde{u}_h]_{\mathbf{n}} + \right. \\ & + (n_r p_j^r) k_\ell [C_{ilhj}^{\mathfrak{A} \setminus \mathfrak{C}}]_{\mathbf{v}} [\tilde{u}_h]_{\mathbf{n}} + (v_r p_j^r) k_\ell [C_{ijh\ell}^{\mathfrak{A} \setminus \mathfrak{C}}]_{\mathbf{v}} [\tilde{u}_h]_{\mathbf{n}} - k_j k_\ell [C_{ijh\ell}^{\mathfrak{A} \setminus \mathfrak{C}}]_{\mathbf{v}} [\tilde{u}_h]_{\mathbf{n}} + (v_r p_j^r) k_\ell r_{ijh\ell}(s) [\chi_{\mathfrak{C}}]_{\mathbf{v}} [\tilde{u}_h]_{\mathbf{n}} + \\ & - (v_r p_j^r)(n_s p_\ell^s) r_{ijh\ell}(s) [\chi_{\mathfrak{C}}]_{\mathbf{v}} [\tilde{u}_h]_{\mathbf{n}} - (n_r p_j^r)(n_s p_\ell^s) r_{ijh\ell}(s) [\chi_{\mathfrak{C}}]_{\mathbf{v}} [\tilde{u}_h]_{\mathbf{n}} + (n_r p_j^r) k_\ell r_{ijh\ell}(s) [\chi_{\mathfrak{C}}]_{\mathbf{v}} [\tilde{u}_h]_{\mathbf{n}} + \\ & \left. + (n_r p_j^r) k_\ell r_{ilhj}(s) [\chi_{\mathfrak{C}}]_{\mathbf{v}} [\tilde{u}_h]_{\mathbf{n}} - k_j k_\ell r_{ijh\ell}(s) [\chi_{\mathfrak{C}}]_{\mathbf{v}} [\tilde{u}_h]_{\mathbf{n}} - [\rho]_{\mathbf{v}} s^2 \delta_{ih} [\tilde{u}_h]_{\mathbf{n}} \right) e^{i(\mathbf{G}(\mathbf{n}) + \mathbf{G}(\mathbf{v})) \cdot \mathbf{x}} = 0. \quad (17) \end{aligned}$$

Defining the multi-index  $\mathbf{m} = \mathbf{v} + \mathbf{n}$ , equation (17) becomes

$$\begin{aligned} \sum_{\mathbf{n} \in \mathbb{Z}^3} \sum_{\mathbf{m} \in \mathbb{Z}^3} & \left( - ((m_r - n_r) p_j^r)(n_s p_\ell^s) [C_{ijh\ell}^{\mathfrak{A} \setminus \mathfrak{C}}]_{\mathbf{m} - \mathbf{n}} [\tilde{u}_h]_{\mathbf{n}} - (n_r p_j^r)(n_s p_\ell^s) [C_{ijh\ell}^{\mathfrak{A} \setminus \mathfrak{C}}]_{\mathbf{m} - \mathbf{n}} [\tilde{u}_h]_{\mathbf{n}} - k_j k_\ell [C_{ijh\ell}^{\mathfrak{A} \setminus \mathfrak{C}}]_{\mathbf{m} - \mathbf{n}} [\tilde{u}_h]_{\mathbf{n}} + \right. \\ & + (n_r p_j^r) k_\ell r_{ijh\ell}(s) [\chi_{\mathfrak{C}}]_{\mathbf{v}} [\tilde{u}_h]_{\mathbf{n}} + (n_r p_j^r) k_\ell r_{ilhj}(s) [\chi_{\mathfrak{C}}]_{\mathbf{m} - \mathbf{n}} [\tilde{u}_h]_{\mathbf{n}} + ((m_r - n_r) p_j^r) k_\ell r_{ijh\ell}(s) [\chi_{\mathfrak{C}}]_{\mathbf{m} - \mathbf{n}} [\tilde{u}_h]_{\mathbf{n}} + \\ & + (n_r p_j^r) k_\ell [C_{ijh\ell}^{\mathfrak{A} \setminus \mathfrak{C}}]_{\mathbf{m} - \mathbf{n}} [\tilde{u}_h]_{\mathbf{n}} + (n_r p_j^r) k_\ell [C_{ilhj}^{\mathfrak{A} \setminus \mathfrak{C}}]_{\mathbf{m} - \mathbf{n}} [\tilde{u}_h]_{\mathbf{n}} + ((m_r - n_r) p_j^r) k_\ell [C_{ijh\ell}^{\mathfrak{A} \setminus \mathfrak{C}}]_{\mathbf{m} - \mathbf{n}} [\tilde{u}_h]_{\mathbf{n}} + \\ & - ((m_r - n_r) p_j^r)(n_s p_\ell^s) r_{ijh\ell}(s) [\chi_{\mathfrak{C}}]_{\mathbf{m} - \mathbf{n}} [\tilde{u}_h]_{\mathbf{n}} - (n_r p_j^r)(n_s p_\ell^s) r_{ijh\ell}(s) [\chi_{\mathfrak{C}}]_{\mathbf{m} - \mathbf{n}} [\tilde{u}_h]_{\mathbf{n}} + \\ & \left. - k_j k_\ell r_{ijh\ell}(s) [\chi_{\mathfrak{C}}]_{\mathbf{m} - \mathbf{n}} [\tilde{u}_h]_{\mathbf{n}} - [\rho]_{\mathbf{m} - \mathbf{n}} s^2 \delta_{ih} [\tilde{u}_h]_{\mathbf{n}} \right) e^{i\mathbf{G}(\mathbf{m}) \cdot \mathbf{x}} = 0. \quad (18) \end{aligned}$$

The infinite-dimensional equation (18) can be rewritten in a more compact form, that is (18) reads

$$\left( \mathbf{A} + s^2 \mathbf{B} + r_{1jh\ell}(s) \mathbf{C}_{1jh\ell} + r_{2jh\ell}(s) \mathbf{C}_{2jh\ell} + r_{3jh\ell}(s) \mathbf{C}_{3jh\ell} \right) \tilde{\mathbf{u}} = \mathbf{0}, \quad (19)$$

where the infinite-dimensional linear operators  $\mathbf{A}$ ,  $\mathbf{B}$  and  $\mathbf{C}_{ijh\ell}$ , with  $i, j, h, \ell = 1, 2, 3$ , defined in terms

of the argument  $\tilde{\mathbf{u}}$  written as

$$\tilde{\mathbf{u}} = \text{col}(\mathbf{u}_1, \mathbf{u}_2, \mathbf{u}_3) \in \ell_2(\mathbb{Z}^3)^3, \quad (20)$$

where  $\mathbf{u}_1, \mathbf{u}_2, \mathbf{u}_3$  are vectors collecting, respectively, the Fourier coefficients  $[\tilde{u}_1]_n, [\tilde{u}_2]_n, [\tilde{u}_3]_n$ , the col operator stacks its vector arguments column-wise into a single column vector,  $\ell_2(\mathbb{Z}^3)$  denotes the space of square-summable sequences with three integer indices and  $\ell_2(\mathbb{Z}^3)^3$  is  $\ell_2(\mathbb{Z}^3) \times \ell_2(\mathbb{Z}^3) \times \ell_2(\mathbb{Z}^3)$ . The operators  $\mathbf{A}$ ,  $\mathbf{B}$  and  $\mathbf{C}_{ijh\ell}$  are detailed in Appendix A. Equation (19) is an infinite-dimensional rational eigenproblem in terms of the complex frequency  $s$  and the polarization vector of the Bloch wave  $\tilde{\mathbf{u}}$ , playing the role of eigenvalue and eigenvector, respectively.

Notice that, by exploiting the symmetries of the tensor  $\hat{\mathbf{C}}_{ijh\ell}$  and, therefore, those of the rational polynomial functions  $r_{ijh\ell}$  as well, the equation (19) takes the form

$$\begin{aligned} & \left( \mathbf{A} + s^2 \mathbf{B} + r_{1111}(s) \mathbf{D}_1 + r_{1112}(s) \mathbf{D}_2 + r_{1113}(s) \mathbf{D}_3 + r_{1122}(s) \mathbf{D}_4 + r_{1123}(s) \mathbf{D}_5 \right. \\ & + r_{1133}(s) \mathbf{D}_6 + r_{1212}(s) \mathbf{D}_7 + r_{1213}(s) \mathbf{D}_8 + r_{1222}(s) \mathbf{D}_9 + r_{1223}(s) \mathbf{D}_{10} \\ & + r_{1233}(s) \mathbf{D}_{11} + r_{1313}(s) \mathbf{D}_{12} + r_{1322}(s) \mathbf{D}_{13} + r_{1323}(s) \mathbf{D}_{14} + r_{1333}(s) \mathbf{D}_{15} \\ & + r_{2223}(s) \mathbf{D}_{16} + r_{2233}(s) \mathbf{D}_{17} + r_{2323}(s) \mathbf{D}_{18} + r_{2333}(s) \mathbf{D}_{19} + r_{2222}(s) \mathbf{D}_{20} \\ & \left. + r_{3333}(s) \mathbf{D}_{21} \right) \tilde{\mathbf{u}} = \mathbf{0}. \end{aligned} \quad (21)$$

where

$$\begin{aligned} \mathbf{D}_1 &= \mathbf{C}_{1111} & \mathbf{D}_2 &= 3\mathbf{C}_{1112} + \mathbf{C}_{2111}, & \mathbf{D}_3 &= 3\mathbf{C}_{1112} + \mathbf{C}_{3111}, & (22) \\ \mathbf{D}_4 &= \mathbf{C}_{1122} + \mathbf{C}_{2211}, & \mathbf{D}_5 &= 2\mathbf{C}_{1123} + \mathbf{C}_{2311} + \mathbf{C}_{3211}, & \mathbf{D}_6 &= \mathbf{C}_{1133} + \mathbf{C}_{3311}, \\ \mathbf{D}_7 &= 2\mathbf{C}_{1212} + 2\mathbf{C}_{2121}, & \mathbf{D}_8 &= 4\mathbf{C}_{1213} + 2\mathbf{C}_{2113} + 2\mathbf{C}_{3112}, & \mathbf{D}_9 &= \mathbf{C}_{1222} + 3\mathbf{C}_{2122}, \\ \mathbf{D}_{10} &= 2\mathbf{C}_{1223} + 4\mathbf{C}_{2123} + 2\mathbf{C}_{3212}, & \mathbf{D}_{11} &= \mathbf{C}_{1233} + \mathbf{C}_{2133} + 2\mathbf{C}_{3312}, & \mathbf{D}_{12} &= 2\mathbf{C}_{1313} + 2\mathbf{C}_{3131}, \\ \mathbf{D}_{13} &= \mathbf{C}_{1322} + 2\mathbf{C}_{2213} + \mathbf{C}_{3122}, & \mathbf{D}_{14} &= 2\mathbf{C}_{1323} + 2\mathbf{C}_{2313} + 4\mathbf{C}_{3123}, & \mathbf{D}_{15} &= \mathbf{C}_{1333} + 3\mathbf{C}_{3133}, \\ \mathbf{D}_{16} &= 3\mathbf{C}_{2223} + \mathbf{C}_{3222}, & \mathbf{D}_{17} &= \mathbf{C}_{2233} + \mathbf{C}_{3322}, & \mathbf{D}_{18} &= 2\mathbf{C}_{2323} + 2\mathbf{C}_{3223}, \\ \mathbf{D}_{19} &= \mathbf{C}_{2333} + 3\mathbf{C}_{3233}, & \mathbf{D}_{20} &= \mathbf{C}_{2222} & \mathbf{D}_{21} &= \mathbf{C}_{3333} \end{aligned}$$

In case the rational polynomial  $r_{ijh\ell}(s)$  is not in a reduced form, the polynomial division

$$r_{ijh\ell}(s) = \frac{n_{ijh\ell}(s)}{q_{ijh\ell}(s)} = d_{ijh\ell}(s) + \frac{p_{ijh\ell}(s)}{q_{ijh\ell}(s)} \quad (23)$$

can be performed, with  $d_{ijh\ell}$ ,  $p_{ijh\ell}$ ,  $q_{ijh\ell}$  polynomials in  $s$  of a certain degree. The eigen-problem (22) can thus be reduced to the form

$$\left( \mathfrak{P}(\mathbf{A}, \mathbf{B}, \mathbf{C}_{ijk\ell}, d_{ijk\ell}(s), s) + \mathfrak{R}(\mathbf{C}_{ijk\ell}, p_{ijk\ell}(s), q_{ijk\ell}(s)) \right) \tilde{\mathbf{u}} = \mathbf{0}, \quad (24)$$

where  $\mathfrak{P}$  is the polynomial part and  $\mathfrak{R}$  is the rational one. The first is defined as

$$\begin{aligned}\mathfrak{P} = & \mathbf{A} + s^2 \mathbf{B} + d_{1111}(s) \mathbf{D}_1 + d_{1112}(s) \mathbf{D}_2 + d_{1113}(s) \mathbf{D}_3 + d_{1122}(s) \mathbf{D}_4 + d_{1123}(s) \mathbf{D}_5 \\ & + d_{1133}(s) \mathbf{D}_6 + d_{1212}(s) \mathbf{D}_7 + d_{1213}(s) \mathbf{D}_8 + d_{1222}(s) \mathbf{D}_9 + d_{1223}(s) \mathbf{D}_{10} \\ & + d_{1233}(s) \mathbf{D}_{11} + d_{1313}(s) \mathbf{D}_{12} + d_{1322}(s) \mathbf{D}_{13} + d_{1323}(s) \mathbf{D}_{14} + d_{1333}(s) \mathbf{D}_{15} \\ & + d_{2223}(s) \mathbf{D}_{16} + d_{2233}(s) \mathbf{D}_{17} + d_{2323}(s) \mathbf{D}_{18} + d_{2333}(s) \mathbf{D}_{19} + d_{2222}(s) \mathbf{D}_{20} \\ & + d_{3333}(s) \mathbf{D}_{21}.\end{aligned}\quad (25)$$

whence, if  $d = \max\{2, \deg(d_{ijh\ell}), \text{ for } i, j, h, \ell = 1, 2, 3\}$ , equation (25) can be written in the form

$$\mathfrak{P} = \mathbf{A}_0 + s\mathbf{A}_1 + \cdots + s^d \mathbf{A}_d. \quad (26)$$

The rational part of the eigen-problem (24) takes the form

$$\begin{aligned}\mathfrak{R} = & \frac{p_{1111}(s)}{q_{1111}(s)} \mathbf{D}_1 + \frac{p_{1112}(s)}{q_{1112}(s)} \mathbf{D}_2 + \frac{p_{1113}(s)}{q_{1113}(s)} \mathbf{D}_3 + \frac{p_{1122}(s)}{q_{1122}(s)} \mathbf{D}_4 + \frac{p_{1123}(s)}{q_{1123}(s)} \mathbf{D}_5 + \frac{p_{1133}(s)}{q_{1133}(s)} \mathbf{D}_6 \\ & + \frac{p_{1212}(s)}{q_{1212}(s)} \mathbf{D}_7 + \frac{p_{1213}(s)}{q_{1213}(s)} \mathbf{D}_8 + \frac{p_{1222}(s)}{q_{1222}(s)} \mathbf{D}_9 + \frac{p_{1223}(s)}{q_{1223}(s)} \mathbf{D}_{10} + \frac{p_{1233}(s)}{q_{1233}(s)} \mathbf{D}_{11} \\ & + \frac{p_{1313}(s)}{q_{1313}(s)} \mathbf{D}_{12} + \frac{p_{1322}(s)}{q_{1322}(s)} \mathbf{D}_{13} + \frac{p_{1323}(s)}{q_{1323}(s)} \mathbf{D}_{14} + \frac{p_{1333}(s)}{q_{1333}(s)} \mathbf{D}_{15} + \frac{p_{2223}(s)}{q_{2223}(s)} \mathbf{D}_{16} \\ & + \frac{p_{2233}(s)}{q_{2233}(s)} \mathbf{D}_{17} + \frac{p_{2323}(s)}{q_{2323}(s)} \mathbf{D}_{18} + \frac{p_{2333}(s)}{q_{2333}(s)} \mathbf{D}_{19} + \frac{p_{2222}(s)}{q_{2222}(s)} \mathbf{D}_{20} + \frac{p_{3333}(s)}{q_{3333}(s)} \mathbf{D}_{21},\end{aligned}\quad (27)$$

which, for simplicity, can be rewritten in compact form as

$$\mathfrak{R} = \sum_{i=1}^{21} \frac{p_i(s)}{q_i(s)} \mathbf{D}_i, \quad (28)$$

where the  $s$ -dependent terms are

$$\begin{aligned}\frac{p_1(s)}{q_1(s)} &:= \frac{p_{1111}(s)}{q_{1111}(s)}, & \frac{p_2(s)}{q_2(s)} &:= \frac{p_{1112}(s)}{q_{1112}(s)}, & \frac{p_3(s)}{q_3(s)} &:= \frac{p_{1113}(s)}{q_{1113}(s)}, & \frac{p_4(s)}{q_4(s)} &:= \frac{p_{1122}(s)}{q_{1122}(s)}, \\ \frac{p_5(s)}{q_5(s)} &:= \frac{p_{1123}(s)}{q_{1123}(s)}, & \frac{p_6(s)}{q_6(s)} &:= \frac{p_{1133}(s)}{q_{1133}(s)}, & \frac{p_7(s)}{q_7(s)} &:= \frac{p_{1212}(s)}{q_{1212}(s)}, & \frac{p_8(s)}{q_8(s)} &:= \frac{p_{1213}(s)}{q_{1213}(s)}, \\ \frac{p_9(s)}{q_9(s)} &:= \frac{p_{1222}(s)}{q_{1222}(s)}, & \frac{p_{10}(s)}{q_{10}(s)} &:= \frac{p_{1223}(s)}{q_{1223}(s)}, & \frac{p_{11}(s)}{q_{11}(s)} &:= \frac{p_{1233}(s)}{q_{1233}(s)}, & \frac{p_{12}(s)}{q_{12}(s)} &:= \frac{p_{1313}(s)}{q_{1313}(s)}, \\ \frac{p_{13}(s)}{q_{13}(s)} &:= \frac{p_{1322}(s)}{q_{1322}(s)}, & \frac{p_{14}(s)}{q_{14}(s)} &:= \frac{p_{1323}(s)}{q_{1323}(s)}, & \frac{p_{15}(s)}{q_{15}(s)} &:= \frac{p_{1333}(s)}{q_{1333}(s)}, & \frac{p_{16}(s)}{q_{16}(s)} &:= \frac{p_{2223}(s)}{q_{2223}(s)}, \\ \frac{p_{17}(s)}{q_{17}(s)} &:= \frac{p_{2233}(s)}{q_{2233}(s)}, & \frac{p_{18}(s)}{q_{18}(s)} &:= \frac{p_{2323}(s)}{q_{2323}(s)}, & \frac{p_{19}(s)}{q_{19}(s)} &:= \frac{p_{2333}(s)}{q_{2333}(s)}, & \frac{p_{20}(s)}{q_{20}(s)} &:= \frac{p_{2222}(s)}{q_{2222}(s)}, \\ \frac{p_{21}(s)}{q_{21}(s)} &:= \frac{p_{3333}(s)}{q_{3333}(s)}.\end{aligned}\quad (29)$$

The infinite-dimensional rational eigenproblem (19) thus results in the suitable form

$$\left( \mathbf{A}_0 + \cdots + \mathbf{A}_d s^d + \sum_{i=1}^{21} \frac{p_i(s)}{q_i(s)} \mathbf{D}_i \right) \tilde{\mathbf{u}} = \mathbf{0}. \quad (30)$$

### 3.2. Spatial damping: complex wave number parameterized by the angular frequency

A second strategy consists in fixing the parameter  $s$  in order to obtain an eigenproblem with respect to the norm of the complex wave vector  $\mathbf{k}$ , denoted as  $k$ . In this way, spatial damping features of the propagating wave are investigated for the material at hand. If  $\boldsymbol{\kappa}$  denotes a versor identifying the direction of the vector  $\mathbf{k}$ , i.e.,  $\boldsymbol{\kappa} = \frac{\mathbf{k}}{\|\mathbf{k}\|}$ , the wave vector vector  $\mathbf{k}$  is  $\mathbf{k} = k\boldsymbol{\kappa}$ , and equation (15) results as

$$\begin{aligned} & \sum_{\mathbf{n} \in \mathbb{Z}^3} \sum_{\mathbf{v} \in \mathbb{Z}^3} \left( - (v_r p_j^r)(n_s p_\ell^s) [\hat{\mathcal{C}}_{ijh\ell}]_{\mathbf{v}} [\tilde{u}_h]_{\mathbf{n}} - (n_r p_j^r)(n_s p_\ell^s) [\hat{\mathcal{C}}_{ijh\ell}]_{\mathbf{v}} [\tilde{u}_h]_{\mathbf{n}} \right. \\ & + k(n_r p_j^r) \kappa_\ell [\hat{\mathcal{C}}_{ijh\ell}]_{\mathbf{v}} [\tilde{u}_h]_{\mathbf{n}} + k(n_r p_j^r) \kappa_\ell [\hat{\mathcal{C}}_{i\ell h j}]_{\mathbf{v}} [\tilde{u}_h]_{\mathbf{n}} \\ & \left. + k(v_r p_j^r) \kappa_\ell [\hat{\mathcal{C}}_{ijh\ell}]_{\mathbf{v}} [\tilde{u}_h]_{\mathbf{n}} - k^2 \kappa_j \kappa_\ell [\hat{\mathcal{C}}_{ijh\ell}]_{\mathbf{v}} [\tilde{u}_h]_{\mathbf{n}} - [\rho]_{\mathbf{v}} s^2 \delta_{ih} [\tilde{u}_h]_{\mathbf{n}} \right) e^{i(\mathbf{G}(\mathbf{n}) + \mathbf{G}(\mathbf{v})) \cdot \mathbf{x}} = 0. \end{aligned} \quad (31)$$

As in the previous case, the multi-index  $\mathbf{m} = \mathbf{v} + \mathbf{n}$  can be introduced, transforming equation (31) in the following

$$\begin{aligned} & \sum_{\mathbf{n} \in \mathbb{Z}^3} \sum_{\mathbf{m} \in \mathbb{Z}^3} \left( - ((m_r - n_r) p_j^r)(n_s p_\ell^s) [\hat{\mathcal{C}}_{ijh\ell}]_{\mathbf{m}-\mathbf{n}} [\tilde{u}_h]_{\mathbf{n}} - (n_r p_j^r)(n_s p_\ell^s) [\hat{\mathcal{C}}_{ijh\ell}]_{\mathbf{m}-\mathbf{n}} [\tilde{u}_h]_{\mathbf{n}} \right. \\ & + k(n_r p_j^r) \kappa_\ell [\hat{\mathcal{C}}_{ijh\ell}]_{\mathbf{m}-\mathbf{n}} [\tilde{u}_h]_{\mathbf{n}} + k(n_r p_j^r) \kappa_\ell [\hat{\mathcal{C}}_{i\ell h j}]_{\mathbf{m}-\mathbf{n}} [\tilde{u}_h]_{\mathbf{n}} + k((m_r - n_r) p_j^r) \kappa_\ell [\hat{\mathcal{C}}_{ijh\ell}]_{\mathbf{m}-\mathbf{n}} [\tilde{u}_h]_{\mathbf{n}} \\ & \left. - k^2 \kappa_j \kappa_\ell [\hat{\mathcal{C}}_{ijh\ell}]_{\mathbf{m}-\mathbf{n}} [\tilde{u}_h]_{\mathbf{n}} - [\rho]_{\mathbf{m}-\mathbf{n}} s^2 \delta_{ih} [\tilde{u}_h]_{\mathbf{n}} \right) e^{i\mathbf{G}(\mathbf{m}) \cdot \mathbf{x}} = 0. \end{aligned} \quad (32)$$

Once again, the equation (32) can be written in a compact form as

$$\left( \mathbf{A}^{(k)} + k\mathbf{B}^{(k)} + k^2\mathbf{C}^{(k)} \right) \tilde{\mathbf{u}} = \mathbf{0}, \quad (33)$$

which defines a quadratic eigenvalue problem in  $k$ , governed by infinite-dimensional algebraic operators  $\mathbf{A}^{(k)}$ ,  $\mathbf{B}^{(k)}$ , and  $\mathbf{C}^{(k)}$ , with the argument  $\tilde{\mathbf{u}}$  defined as in (20) and detailed in Appendix B.

## 4. Truncation of the infinite-dimensional eigen-problem

The eigenproblems (30) and (33) are infinite-dimensional algebraic systems of equation, in order to find an approximate solution of these eigen-problems the system might be truncated by considering the multi-indices  $\mathbf{m}$  and  $\mathbf{n}$  which satisfy  $\|\mathbf{m}\|_\infty, \|\mathbf{n}\|_\infty \leq N$  for a certain  $N \in \mathbb{N}^{>0}$ , with  $\|\cdot\|_\infty$  being the infinity norm. As a consequence, the infinite operators in the compact form (54)-(56) and (57)-(59) of both settings are replaced by the corresponding finite-dimensional operators, that are matrices, denoted by the apex  $(f)$ . Therefore, using the same notation of (24) for the first case, the corresponding

finite-dimensional problems take the form

$$\left(\mathfrak{P}^{(f)}(\mathbf{A}^{(f)}, \mathbf{B}^{(f)}, \mathbf{C}_{ijk\ell}^{(f)}, d_{ijk\ell}(s), s) + \mathfrak{R}^{(f)}(\mathbf{C}_{ijk\ell}^{(f)}, p_{ijk\ell}(s), q_{ijk\ell}(s))\right) \tilde{\mathbf{u}}^{(f)} = \mathbf{0}, \quad (34)$$

and

$$\left(\mathbf{A}^{(k),(f)} + k\mathbf{B}^{(k),(f)} + k^2\mathbf{C}^{(k),(f)}\right) \tilde{\mathbf{u}}^{(f)} = \mathbf{0}, \quad (35)$$

where the vector  $\tilde{\mathbf{u}}^{(f)}$  contains the finite-dimensional Fourier coefficients of the Bloch amplitude components. In the case of spatial damping, the problem (35) can be solved through standard numerical techniques for quadratic eigenproblems or their linearized version. The finite-dimensional rational eigenproblem of a tri-dimensional problem involves matrices of dimension  $2M_N \times 2M_N$  with  $M_N = (2N+1)^3$ . However, due to the multi-indices  $\mathbf{m} - \mathbf{n}$  a greater amount of Fourier coefficients need to be computed, specifically, the coefficients related to the indices  $\|\mathbf{m} - \mathbf{n}\| \leq 2N$  must be computed, which means to determine  $(4N+1)^3$  coefficients. Heterogeneous architected materials which are characterized by periodic piecewise constant functions  $\hat{C}_{ijh\ell}$  and  $\rho$ , might present the Gibbs phenomenon when represented by Fourier series, since it causes inaccuracies in their descriptions. To address this, it has been developed various mitigation methods, including polynomial and rational interpolations, as well as combinations of Fourier series with regularization filters [45, 58–63]. These techniques aim to improve the accuracy of the models.

#### 4.1. Derationalization of the finite-dimensional rational eigen-problem

For the temporal damping case, the eigenproblem (35) has a rational nature. It can be solved as a generic nonlinear eigenproblem by determining the roots of the associated characteristic equation, or it can be tackled with suitable derationalization techniques, which transform the rational eigenproblem into a polynomial form that is generally more tractable. In particular, an improved derationalization method can be employed. This technique converts the rational eigenproblem into a linear eigenproblem of slightly increased dimensions, which is typically easier to solve. From a computational standpoint, due to the size of the matrices involved, this approach can be more advantageous than the standard derationalization procedure which relies on multiplying the rational problem by the product of denominators. It can lead to bigger matrices, particularly when the degree of denominators is greater than one. One considers a generic finite-dimensional eigen-problem that consists of a polynomial and a rational part, that is the eigenproblem

$$\left(\mathbf{A}_0^{(f)} + \dots \mathbf{A}_d^{(f)} s^d + \sum_{i=1}^k \frac{p_i(s)}{q_i(s)} \mathbf{D}_i^{(f)}\right) \tilde{\mathbf{u}}^{(f)} = \mathbf{0}, \quad (36)$$

for a certain integer  $k \geq 1$ , and where  $\mathbf{A}_j^{(f)}$  and  $\mathbf{D}_i^{(f)}$  are square matrices of size  $n \times n$ ,  $\tilde{\mathbf{u}}^{(f)}$  the related eigenvector of size  $n$  and  $p_i, q_i$  are polynomials of certain degrees which are assumed to be written in a reduced form such that the leading coefficient of the denominators  $q_i$  is one. Then, it is possible to



write it as a product of matrices (see e.g. [64]) as

$$\frac{p_i(s)}{q_i(s)} = (\mathbf{a}_i^{(f)})^T (s\mathbf{I}_1^{(f)} - \mathbf{E}_i^{(f)})^{-1} \mathbf{b}_i^{(f)} \quad (37)$$

with

$$\mathbf{a}_i^{(f)} = \begin{pmatrix} p_i^{(0)} \\ p_i^{(1)} \\ \vdots \\ p_i^{(v)} \end{pmatrix}^T, \quad \mathbf{E}_i^{(f)} = \begin{pmatrix} 0 & 1 & 0 & 0 \\ 0 & 0 & 1 & 0 \\ \vdots & \vdots & \vdots & \ddots \\ 0 & 0 & 0 & 1 \\ -q_i^{(0)} & -q_i^{(1)} & -q_i^{(2)} & \dots & -q_i^{(v)} \end{pmatrix}, \quad \mathbf{b}_i^{(f)} = \begin{pmatrix} 0 \\ 0 \\ \vdots \\ 0 \\ 1 \end{pmatrix}, \quad (38)$$

and  $\mathbf{I}_1^{(f)}$  the identity matrix of the same size of  $\mathbf{E}_i^{(f)}$ . Therefore, the rational eigen-problem (36) can be properly rearranged by exploiting (37) and  $LU$  decompositions (or rank revealing  $LU$  decomposition to reduce the size of the problem) of the matrices  $\mathbf{D}_i^{(f)}$ , i.e.  $\mathbf{D}_i^{(f)} = \mathbf{L}_i^{(f)} \mathbf{U}_i^{(f)T}$ . The eigen-value problem can thus be rewritten as

$$\left( \mathbf{A}_0^{(f)} + \dots \mathbf{A}_d^{(f)} s^d + \mathbf{L}^{(f)} (s\mathbf{F}^{(f)} - \mathbf{G}^{(f)})^{-1} (\mathbf{U}^{(f)})^T \right) \tilde{\mathbf{u}}^{(f)} = 0, \quad (39)$$

where

$$\begin{aligned} \mathbf{L}^{(f)} &= [\mathbf{L}_1^{(f)} (\mathbf{I}_2^{(f)} \otimes \mathbf{a}_1^{(f)})^T, \dots, \mathbf{L}_k^{(f)} (\mathbf{I}_2^{(f)} \otimes \mathbf{a}_k^{(f)})^T], \\ \mathbf{F}^{(f)} &= \text{diag}(\mathbf{I}_2^{(f)} \otimes \mathbf{I}_1^{(f)}, \dots, \mathbf{I}_2^{(f)} \otimes \mathbf{I}_1^{(f)}), \\ \mathbf{G}^{(f)} &= \text{diag}(\mathbf{I}_2^{(f)} \otimes \mathbf{E}_1^{(f)}, \dots, \mathbf{I}_2^{(f)} \otimes \mathbf{E}_k^{(f)}), \\ \mathbf{U}^{(f)} &= [\mathbf{U}_1^{(f)} (\mathbf{I}_2^{(f)} \otimes \mathbf{b}_1^{(f)})^T, \dots, \mathbf{U}_k^{(f)} (\mathbf{I}_2^{(f)} \otimes \mathbf{b}_k^{(f)})^T]. \end{aligned} \quad (40)$$

and with  $\mathbf{I}_2^{(f)}$  the identity matrix of the size of the matrix  $\mathbf{D}_i^{(f)}$  (or the rank in the case of the rank revealing decomposition), the symbol  $\otimes$  the Kronecker product. Finally, the problem can be linearized in the form

$$(\mathbf{M}^{(f)} - s\mathbf{N}^{(f)}) \mathbf{y}^{(f)} = 0. \quad (41)$$

with certain matrices  $\mathbf{M}^{(f)}$  and  $\mathbf{N}^{(f)}$  of size

$$\varsigma_e = 2M_N(P_e + \sum_{i=1}^k \deg(q_i)) \times 2M_N(P_e + \sum_{i=1}^k \deg(q_i)),$$

with  $P_e = \max\{2, \deg(p_i), i = 1, \dots, k\}$ . This value is significantly smaller than the dimensions of matrices that would result from applying a standard derationalization approach to obtain a polynomial eigenproblem which is

$$\varsigma_s = 2M_N P_s \times 2M_N P_s,$$

with  $P_s = \max\{2 \prod_{i=0}^k \deg(q_i), \deg(p_j) \prod_{i=0}^k \deg(q_i), j = 1, \dots, k\}$ . More details on the procedure can be found in [43].

## 5. Quasi-Monte Carlo integration scheme for the approximation of Fourier coefficients

For complex microstructural topologies, it is difficult to compute the Fourier coefficients in equations (13) and (14) analytically. Cubature formulas can thus be exploited to approximate them. Cubature formulas, exact on algebraic polynomials, involve a better knowledge of the structure or force to split (and approximate) it in tetrahedrons which could increase the computational cost. Hence, it could be preferable to use a Monte Carlo (MC) method [65], which approximates the integral of a function  $f$  on a certain domain  $\Omega$  via the mean value of the function evaluation on random points  $\mathbf{x}_i \in \Omega$  for  $i = 1, \dots, N$ , i.e.,

$$\int_{\Omega} f(\mathbf{x}) \, d\mathbf{x} \approx \frac{|\Omega|}{N} \sum_{i=1}^N f(\mathbf{x}_i), \quad (42)$$

with  $|\Omega|$  the measure of the domain. Once the points are deterministic instead of random the method is called quasi-Monte Carlo (qMC). It has the advantage of having a faster rate of convergence, being the rate of convergence of MC of  $O(N^{-1/2})$ , whereas qMC may converge to a rate of  $O(N^{-1}(\log N)^d)$ . A good choice for the sequence of points is the one where the points are uniformly distributed with respect to the measure  $d\mathbf{x}$ , which means the sequence of points such that

$$\lim_{N \rightarrow \infty} \frac{|\Omega|}{N} \sum_{i=1}^N f(\mathbf{x}_i) = \int_{\Omega} f(\mathbf{x}) \, d\mathbf{x}. \quad (43)$$

Dealing with finite points sets  $\mathcal{X}_N$ , a way to measure the deviation from the uniform distribution consists in the notion of discrepancy. There are many notions of discrepancy depending on the domain of integration  $\Omega$ . In the following, the periodic cube of dimension  $d$  is considered as the domain and it is denoted as  $I^d$ . In an arbitrary subset  $B \subset I^d$ , the counting function  $\#(B, \mathcal{X}_N)$  is defined. It consists of the number of points  $\mathbf{x}_i \in \mathcal{X}_N$  that are contained in  $B$ . Then, a notion of discrepancy of the points set  $\mathcal{X}_N$  is given by considering a family of subset  $\mathcal{B}$  in  $I^d$  and measuring how the points set describe the measure of the elements of  $\mathcal{B}$ , i.e.,

$$D_N(\mathcal{B}, \mathcal{X}_N) = \sup_{B \in \mathcal{B}} \left| \frac{\#(B, \mathcal{X}_N)}{N} - |B| \right|, \quad (44)$$

where  $|B|$  denotes the measure of  $B$ .

Choosing different non-empty families of Lebesgue-measurable subsets  $\mathcal{B}$ , makes it possible to define different notions of discrepancy. In case  $\mathcal{B}$  is the family of all the subintervals of the form  $\prod_{i=0}^d [0, u_i]$ , which are all the rectangles pinned in the origins, it is called *star discrepancy* and denoted as  $D_N^*$ .

**Theorem 5.1** (Koksma-Hlawka inequality). *If  $f$  is function with bounded variation  $V(f)$  in the sense of Hardy and Krause [65, p. 20] in  $I^d$ , then for any  $\mathcal{X}_N = \{\mathbf{x}_1, \dots, \mathbf{x}_N\} \subset I^d$ , one has*

$$\left| \frac{1}{N} \sum_{i=1}^N f(\mathbf{x}_i) - \int_{I^d} f(\mathbf{x}) \, d\mathbf{x} \right| \leq V(f) D_N^*(\mathcal{X}_N), \quad (45)$$

where  $D_N^*$  is the star discrepancy of the points set.

This is an important error estimate for qMC method. It states that once the function is fixed, the way for obtaining a better convergence is to use a distribution of points such that the discrepancy is as small as possible. Similar inequalities exist also for different settings such as convex sets [66], or general manifolds [66, 67] where other kinds of discrepancies are used which suit better the geometry of the domain of integration. Once a parametrization of the manifold is known, it is possible to try to transpose the problem by distributing the points well in the parameter sets, as done in [68].

Therefore, the qMC method could be helpful whenever there is the need to compute integrals over geometries for which the analytical calculation is not a practicable way and for which an indomain function can be built, allowing to differentiate which points belong inside the domain and which ones are outside.

Moreover, a good approximation clearly depends on the number of points used. Then, in case of a function  $f$  whose evaluation is computationally expensive, it could be worth considering a compression method, similar to the one recently used in [69], applied to qMC method [70–72]. Our goal then, is to use qMC to approximate the Fourier coefficients in such domains. An approximation is obtained by computing

$$[f]_v := \frac{1}{|\mathfrak{A}|} \int_{\mathfrak{A}} f(\mathbf{x}) e^{-i\mathbf{G}(\mathbf{v}) \cdot \mathbf{x}} d\mathbf{x} \approx \frac{1}{N} \sum_{j=0}^N f(\mathbf{x}_j) e^{-i\mathbf{G}(\mathbf{v}) \cdot \mathbf{x}_j} = \widetilde{[f]}_v, \quad (46)$$

for a sequence of points  $\mathbf{x}_j, j = 0, \dots, N$  with a low discrepancy value in  $\mathfrak{A}$ . In particular, in the case of volume integrals, a low-discrepancy sequence can be used such as the well-known Sobol sequence or Halton sequence which have a star-discrepancy such that

$$D_N^*(\mathcal{X}_N) \leq C \frac{(\log N)^d}{N}, \quad (47)$$

for a certain constant  $C$  which depends on the sequence (see, e.g., [65, p. 29]).

A straightforward estimate of the error of the complete Fourier series with respect to the truncated one and with the coefficients approximated by qMC method consists in the following.

**Proposition 5.2.** *Let us consider the Fourier series  $S[f] = \sum_{\mathbf{v} \in \mathbb{Z}^3} [f]_v e^{i\mathbf{G}(\mathbf{v}) \cdot \mathbf{x}}$  and  $S_N[\widetilde{f}]$  the truncated series with coefficients approximated by qMC, then*

$$\left| S[f] - S_N[\widetilde{f}] \right| \leq \mathcal{E}_{trun} + (2N + 1)^3 \max_{\|\mathbf{v}\| \leq N} \mathcal{E}_{qMC}([f]_v), \quad (48)$$

where  $\mathcal{E}_{trun}$  is the truncation error

$$\mathcal{E}_{tru} = \left| \sum_{\mathbf{v} \in \mathbb{Z}^3} [f]_v e^{i\mathbf{G}(\mathbf{v}) \cdot \mathbf{x}} - \sum_{\|\mathbf{v}\| \leq N} [f]_v e^{i\mathbf{G}(\mathbf{v}) \cdot \mathbf{x}} \right|, \quad (49)$$

and  $\mathcal{E}_{qMC}([f])$  is the error given by the quasi-Monte Carlo approximation of the integral

$$\mathcal{E}_{qMC}([f]) = \left| \frac{1}{|\mathfrak{U}|} \int_{\mathfrak{U}} f(\mathbf{x}) e^{-i\mathbf{G}(\mathbf{v}) \cdot \mathbf{x}} d\mathbf{x} - \frac{1}{N} \sum_{j=0}^N f(\mathbf{x}_j) e^{-i\mathbf{G}(\mathbf{v}) \cdot \mathbf{x}_j} \right|. \quad (50)$$

*Proof.* In fact, by adding and subtracting the truncated series  $S_N[f] = \sum_{\|\mathbf{v}\| \leq N} [f]_{\mathbf{v}} e^{i\mathbf{G}(\mathbf{v}) \cdot \mathbf{x}}$  to the error one has

$$\begin{aligned} \left| S[f] - S_N[\tilde{f}] \right| &\leq \left| S[f] - S_N[f] + S_N[f] - S_N[\tilde{f}] \right| \\ &\leq \mathcal{E}_{trun} + \left| \sum_{\|\mathbf{v}\| \leq N} ([f]_{\mathbf{v}} - [\tilde{f}]_{\mathbf{v}}) e^{i\mathbf{G}(\mathbf{v}) \cdot \mathbf{x}} \right| \\ &\leq \mathcal{E}_{trun} + \max_{\|\mathbf{v}\| \leq N} |[f]_{\mathbf{v}} - [\tilde{f}]_{\mathbf{v}}| \left| \sum_{\|\mathbf{v}\| \leq N} e^{i\mathbf{G}(\mathbf{v}) \cdot \mathbf{x}} \right| \\ &\leq \mathcal{E}_{trun} + \max_{\|\mathbf{v}\| \leq N} \mathcal{E}_{qMC}([f]_{\mathbf{v}}) \left| \sum_{\|\mathbf{v}\| \leq N} e^{i\mathbf{G}(\mathbf{v}) \cdot \mathbf{x}} \right| \\ &\leq \mathcal{E}_{trun} + \max_{\|\mathbf{v}\| \leq N} \mathcal{E}_{qMC}([f]_{\mathbf{v}}) \sum_{\|\mathbf{v}\| \leq N} |e^{i\mathbf{G}(\mathbf{v}) \cdot \mathbf{x}}| \\ &\leq \mathcal{E}_{trun} + (2N + 1)^3 \max_{\|\mathbf{v}\| \leq N} \mathcal{E}_{qMC}([f]_{\mathbf{v}}) \end{aligned} \quad (51)$$

□

From this estimate and from the fact that qMC with  $M$  points allows convergence of the order  $O(M^{-1}(\log M)^d)$ , it can be deduced that the error of the series with approximated coefficients is of a similar order of the one with only the truncated terms as long as the coefficients are approximated with a number of points  $M \gg N^3$ . This means that once enough points are used in the qMC approximation, the series can be treated as the truncated one. A further assessment of the accuracy of the Fourier coefficient approximation obtained through the quasi-Monte Carlo integration scheme is provided in Appendix D. A comparison is presented between the exact analytical computation of the test-case coefficients and their corresponding qMC approximations, for a cubic periodic cell containing an inclusion of the same shape.

## 6. Illustrative example of a viscoelastic TPMS-based architected material

Recent advancements in additive manufacturing have enabled the creation of metamaterials with exceptional mechanical, acoustic, and photonic properties [73–75]. However, strut-based lattice structures present an inconvenient low surface area to volume fraction ratio and moderately low curvature in their internal surface, which are both critical features in industrial and biomedical applications [76]. Among the shell-based metamaterials, the triply periodic minimal surface (TPMS) structures have solved the problem of lightness accompanied by high curvature and surface area [77]. The TPMS are bicontinuous, infinitely-extending saddle-shaped surfaces that locally minimize the area and have the

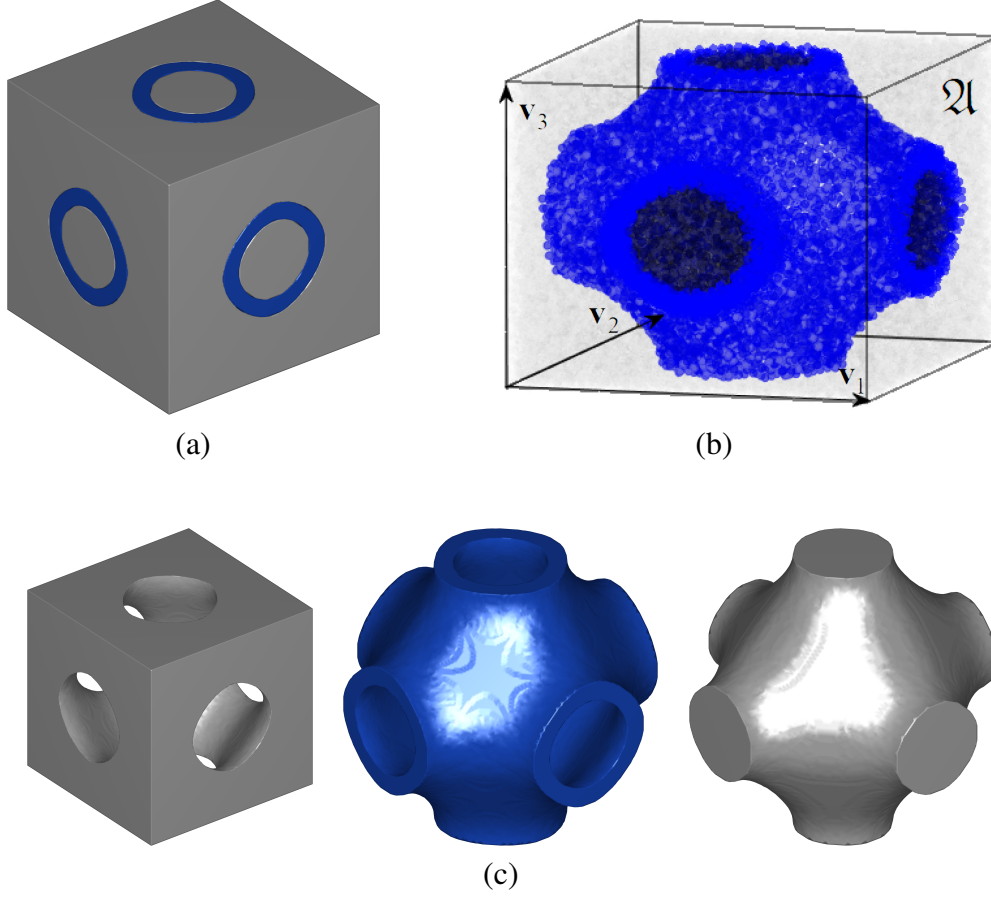


Figure 1: Visualization of the periodic cell  $\mathcal{U}$  used in the Bloch wave analysis. (a) Geometric model of the primitive TPMS-based periodic cell, consisting of an inner matrix core, a surrounding TPMS layer, and an outer matrix, all embedded in a periodic cubic domain defined by the vectors  $\mathbf{v}_1$ ,  $\mathbf{v}_2$ , and  $\mathbf{v}_3$ . (b) Point cloud visualization of the same periodic cell, showing the integration nodes generated via the quasi-Monte Carlo method based on Sobol sequence. (c) Exploded view of the three distinct material subdomains: the outer matrix (gray), the TPMS layer (blue), and the inner matrix (light gray).

peculiar feature of zero mean curvature at every point along the surface [78]. Architected materials based on TPMS have attracted much attention because of their mathematically controlled topologies and excellent physical and mechanical properties. The recent and widespread interest in the design of such metamaterials has regarded different applications, from structural to biomedical ones, especially in tissue engineering [79, 80]. There are four main types of TPMS-based periodic cells, all taking inspiration from natural elements and all periodic along three principal directions, namely the gyroid, inspired by the microstructure of the butterfly wings [81], the primitive, inspired by the microstructure of the sea urchin [82], the diamond, from the molecular structure of a diamond [83], and the IWP, from soap films [84].

This illustrative example investigates the propagation of damped Bloch waves in a periodic material based on a Primitive TPMS (triply periodic minimal surface) topology. This surface features a complex, interconnected geometry, making it attractive for mechanical applications requiring both low weight and high mechanical performance. The analyzed periodic cell, shown in Fig. 1, is cubic with edge length  $d = 10^{-2}$  m and is characterized by the three periodicity vectors  $\mathbf{v}_1$ ,  $\mathbf{v}_2$ , and  $\mathbf{v}_3$ . The mid-surface of the Primitive TPMS was first constructed using the zero-level set of a trigonometric

function, specifically defined as:

$$f(\mathbf{x}) = \sin\left(\frac{2\pi x_1}{d} - \frac{\pi}{2}\right) + \sin\left(\frac{2\pi x_2}{d} - \frac{\pi}{2}\right) + \sin\left(\frac{2\pi x_3}{d} - \frac{\pi}{2}\right). \quad (52)$$

The surface was then symmetrically extruded inward and outward to define a finite-thickness layer. This thickness is implicitly controlled by the two scalar thresholds  $f_1 = 5/100$  and  $f_2 = 5/10$ , which delimit the region of interest where the TPMS scalar field satisfies  $f_1 \leq f(\mathbf{x}) \leq f_2$ . As a result, three distinct material regions are identified: the inner matrix ( $f < f_1$ ), the TPMS layer ( $f_1 \leq f \leq f_2$ ), and the outer embedding matrix ( $f > f_2$ ), see Fig. 1(c). The TPMS structure is modeled as a steel phase, embedded in a viscoelastic epoxy matrix, which occupies the complementary inner and outer regions of the domain. The steel component is modeled as a linear elastic isotropic material with Young's modulus  $E = 210$  GPa, Poisson's ratio  $\nu = 0.3$ , and mass density  $\rho = 7500$  kg/m<sup>3</sup>. The epoxy matrix follows a linear viscoelastic isotropic law, with  $E = 3.6$  GPa,  $\nu = 0.35$ , and  $\rho = 1150$  kg/m<sup>3</sup> [85]. The components of the long-term response tensor  $\mathbb{G}^\infty$  are given by  $G_{ijhk}^\infty = \frac{\nu E}{(1+\nu)(1-2\nu)} \delta_{ij} \delta_{hk} + \frac{E}{2(1+\nu)} (\delta_{ih} \delta_{jk} + \delta_{ik} \delta_{jh})$ , where  $\delta_{ij}$  denotes the Kronecker delta. The points visible in the Fig. 1(b) correspond to the integration nodes used in the numerical simulations, generated through the quasi-Monte Carlo (qMC) approach described in Section 5, in this case specifically based on deterministic Sobol sequences. In particular, the construction of these sequences is detailed in Appendix C. In what follows, the effects of viscous dissipation on the wave propagation characteristics of the system are investigated, with particular focus on both temporal and spatial damping mechanisms. Figs 2 and 3 refer to the investigation of the temporal damping of a homogeneous wave inside the metamaterial, as described in Section 3.1, for which the wave vector  $\mathbf{k}$  is a real parameter and the complex frequency  $s$  represents the eigenvalue of a rational eigenproblem, derationalized by the procedure detailed in Section 4.1. In particular, setting once and for all the viscosity ratios  $\gamma^n = 1$  in the Prony series (1), Fig. 2 refers to the case in which one single term has been considered ( $N=1$ ) with relaxation time  $\tau_r^1 \omega_{ref} = 10^{-5}$ , while Fig. 3 refers to the case in which  $N = 2$ , with  $\tau_r^1 \omega_{ref} = 10^{-2}$  and  $\tau_r^2 \omega_{ref} = 10^{-4}$ . The reference frequency  $\omega_{ref}$  has been set equal to  $\omega_{ref} = d^{-1} \sqrt{\frac{E}{\rho}}$ , with  $E$  and  $\rho$  of the steel phase. Setting the direction of propagation  $\mathbf{n} = \mathbf{e}_1$ , Figs 2-(a) and 3-(a) represent the obtained three-dimensional Floquet-Bloch spectra plotted in terms of the first dimensionless wave vector component  $\bar{k}_1 = k_1 d$  in the range  $[0, \pi]$  and the real and imaginary components of the dimensionless complex frequency  $\bar{s} = \bar{s}_r + i \bar{s}_i = s / \omega_{ref}$ . The real component  $\bar{s}_r$  is associated with the wave's dissipation and, as expected, its values are greater in the case  $N = 1$  with respect to the case  $N = 2$ . Instead, the imaginary component  $\bar{s}_i$  is related to the wave propagation. It should be noted that, given the cubic symmetry of the considered periodic cell, the same spectrum would have been obtained along  $\mathbf{e}_2$  or  $\mathbf{e}_3$ . In the case of two relaxation times, the spectral density of the optical branches increases a lot for values of  $\bar{s}_i$  greater than 0.15. A further representation of dispersion curves is given in Figs 2-(b),(c) and 3-(b),(c) where the real and imaginary components of  $\bar{\mu} = \exp(\bar{s} \bar{\tau})$ , with  $\bar{\tau} = t \omega_{ref}$  and  $t$  the time variable, are plot in terms of  $\bar{k}_1$ . Specifically, sub-Figs (b) refer to  $\bar{\tau} = 5$ , while sub-Figs (c) to  $\bar{\tau} = 50$ . It can be noted that, for short times, the curves occupy a small portion of the unit

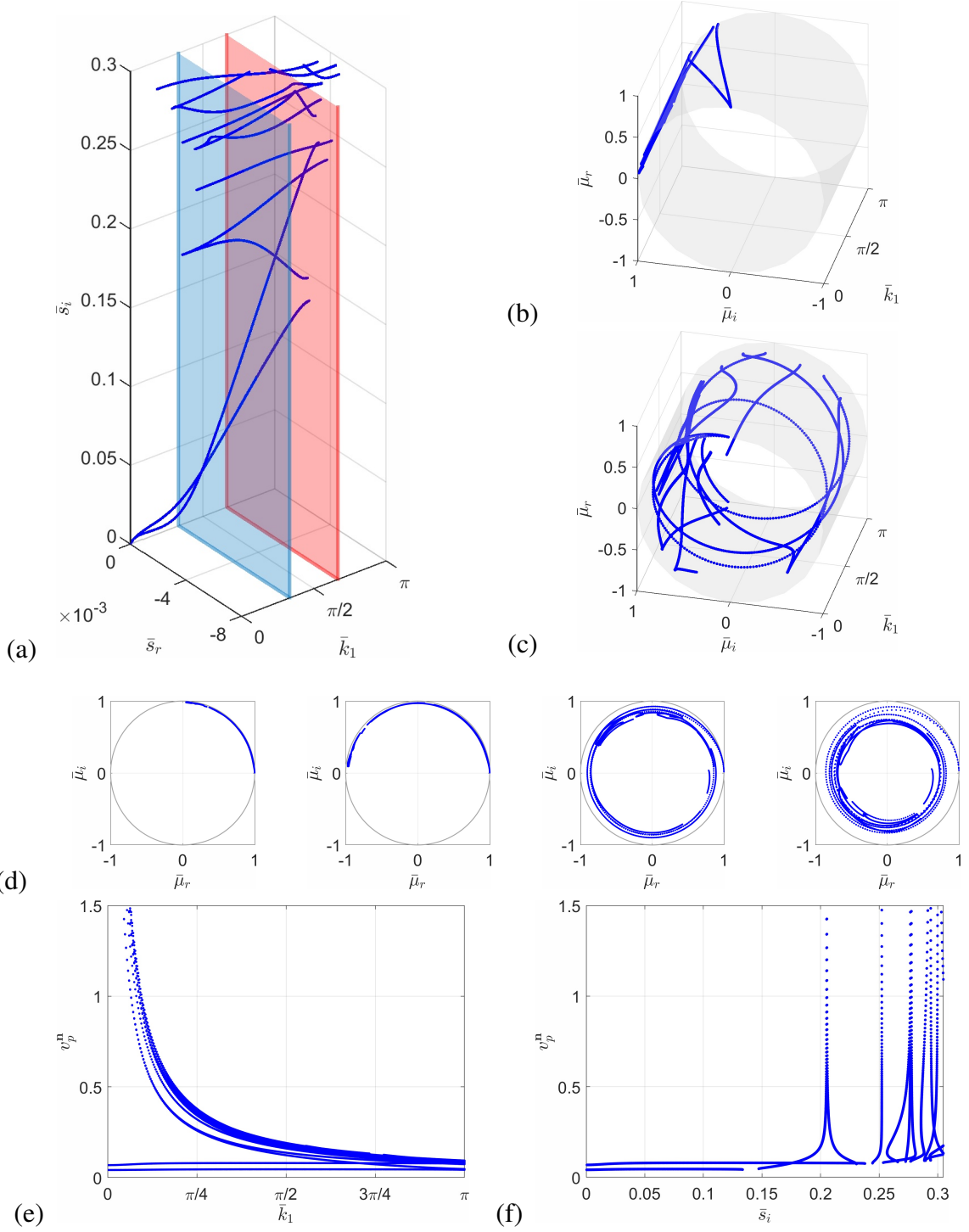


Figure 2: Analysis of temporal damping in the case of  $N=1$  with relaxation time  $\tau_r^1 \omega_{ref} = 10^{-5}$  and  $\omega_{ref} = d^{-1} \sqrt{\frac{E}{\rho}}$ , evaluated with respect to the steel phase. (a) Full three-dimensional representation of the complex dispersion curves for waves propagating along  $\mathbf{n} = \mathbf{e}_1$ . (b) Dispersion curves plotted on the unit cylindrical surface in terms of the real part of the normalized frequency  $\bar{\mu}$  for dimensionless time  $\bar{\tau} = t \omega_{ref} = 5$ . (c) Same as (b) but for  $\bar{\tau} = 50$ . (d) Comparison of dispersion curves on the unit circle for different dimensionless times  $\bar{\tau} = 5, 10, 50, 100$ , showing the effect of increasing viscous dissipation. (e) Magnitude of the phase velocity  $v_p^n$  as a function of the normalized wavenumber  $\bar{k}_1$ . (f) Same quantity plotted with respect to the imaginary part of the complex frequency  $\bar{s}_i$ .

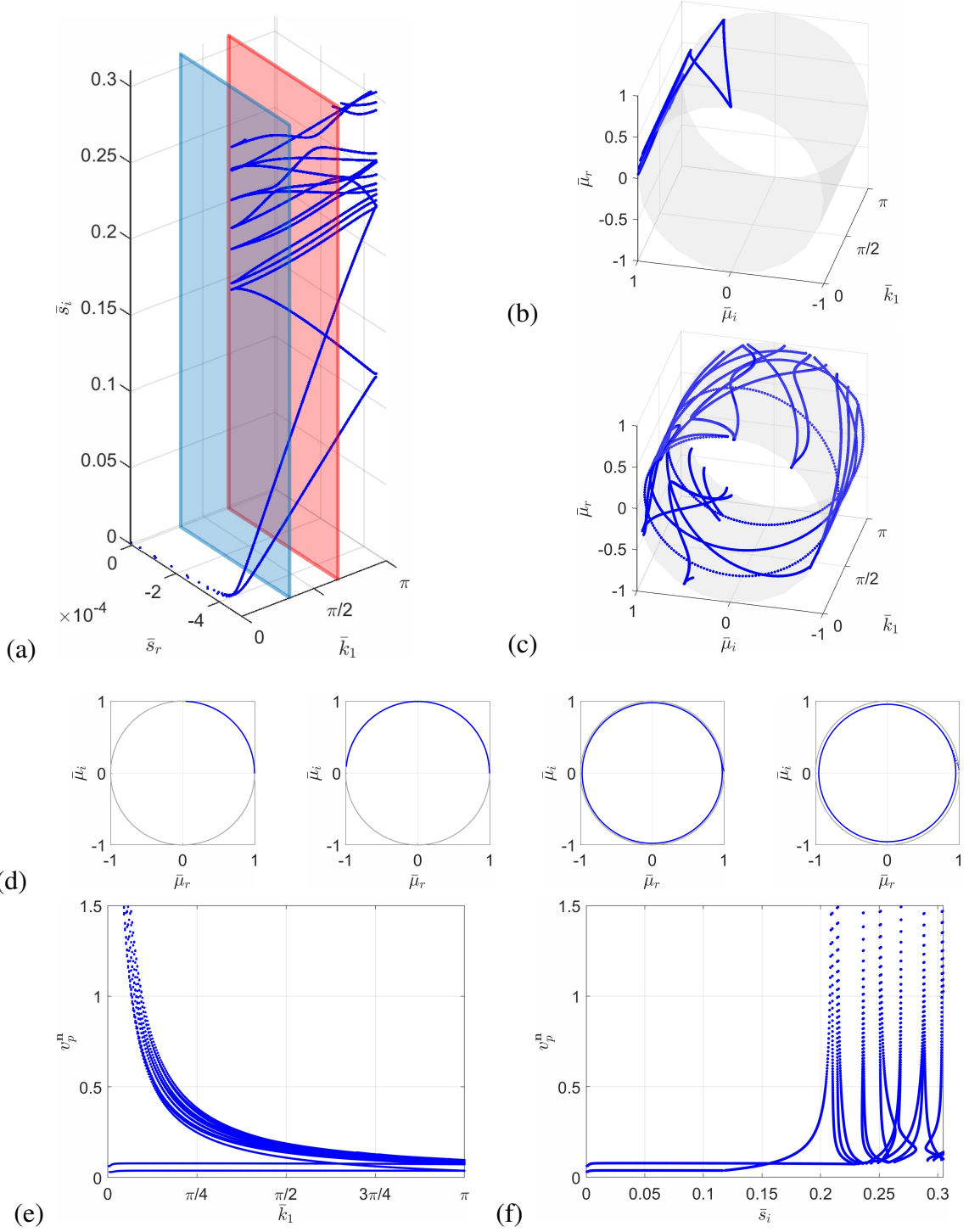


Figure 3: Analysis of temporal damping in the case of  $N=2$  with relaxation times  $\tau_r^1 \omega_{ref} = 10^{-2}$ ,  $\tau_r^2 \omega_{ref} = 10^{-4}$  and  $\omega_{ref} = d^{-1} \sqrt{\frac{E}{\rho}}$ , evaluated with respect to the steel phase. (a) Full three-dimensional representation of the complex dispersion curves for waves propagating along  $\mathbf{n} = \mathbf{e}_1$ . (b) Dispersion curves plotted on the unit cylindrical surface in terms of the real part of the normalized frequency  $\bar{\mu}$  for dimensionless time  $\bar{\tau} = t \omega_{ref} = 5$ . (c) Same as (b) but for  $\bar{\tau} = 50$ . (d) Comparison of dispersion curves on the unit circle for different dimensionless times  $\bar{\tau} = 5, 10, 50, 100$ , showing the effect of increasing viscous dissipation. (e) Magnitude of the phase velocity  $v_p^n$  as a function of the normalized wavenumber  $\bar{k}_1$ . (f) Same quantity plotted with respect to the imaginary part of the complex frequency  $\bar{s}_i$ .



cylinder, while as time increases the curves begin to wrap around the cylinder and then enter inside it, a sign that dissipation has begun to take place. The dissipation mechanisms occur earlier and are more pronounced for the case plotted in Fig. 2 with respect to the case represented in Fig. 3 because of the different values of  $\tau_r^1$ . A confirmation of this is given in the two-dimensional representations 2-(d) and 3-(d), where dispersion curves are plotted for four different times, namely  $\bar{\tau} = 5, 10, 50, 100$ . As time passes, the curves tend to wrap more and more inside the unit cylinder.

To investigate the influence of viscous dissipation on dispersion properties of the damped Bloch wave traveling along direction  $\mathbf{n} = \mathbf{k}/\|\mathbf{k}\|_2$ , the phase velocity vector is defined as  $\mathbf{v}_p^n := \bar{s}_i/\bar{k}_1 \mathbf{n}$ . Its magnitude  $v_p^n := \|\mathbf{v}_p^n\|_2/(\omega_{ref}d) = \bar{s}_i/\bar{k}_1$  is the imaginary component of the complex velocity  $v_c = \bar{s}/\bar{k}_1$  [86]. It represents the velocity at which the phase of any harmonic component of the wave travels. Still, it also represents the projection of the energy velocity vector  $\mathbf{v}_e$ , which defines the location of the wave surface associated with each frequency component, and of the velocity vector related to the dissipated energy  $\mathbf{v}_d$  onto the propagation direction, namely  $\mathbf{n} \cdot \mathbf{v}_e = v_p^n$  and  $\mathbf{n} \cdot \mathbf{v}_d = v_p^n$ . Figs 2-(e) and 3-(e) plot the magnitude of the phase velocity  $v_p^n$  as a function of the dimensionless wave vector component  $\bar{k}_1$ . It is observed that the two curves with lower phase velocity have an almost constant behavior in terms of  $\bar{k}_1$ . They are associated with the acoustic branches of the spectrum. All the other curves, which are associated with the optical branches, show a monotonically decreasing behavior as  $\bar{k}_1$  increases, namely moving from long to short-wave regime. The magnitude of the phase velocity is also represented in Fig. 2-(f) and 3-(f) as a function of  $\bar{s}_i$ . Once again, the two curves at the lowest frequencies are associated with the two acoustic branches of the spectrum, showing finite values of  $v_p^n$ . The remaining curves at higher frequencies are associated with the optical branches of the spectrum, exhibiting vertical asymptotes corresponding to infinite velocity values. Furthermore, pass and stop bands of the corresponding spectrum are recognizable along abscissa  $\bar{s}_i$ .

Without losing generality and focusing the attention on the case  $N = 1$ , the periodic material exhibits a non-monotonic damping behavior as relaxation time increases, as plotted in Fig. 4. This kind of behavior has been previously observed by the authors for different metamaterials [37, 43, 87]. The real and imaginary components of dimensionless frequency  $\bar{s}$  are plotted in Fig. 4 in terms of the dimensionless relaxation time  $\tau_r\omega_{ref}$  for two different values of  $k_1d$ , namely  $k_1d = \pi/3$  and  $k_1d = 2\pi/3$ , that are the values correspondent to the planes drawn in Fig. 2-(a). As  $\tau_r\omega_{ref}$  increases, the curves of Figs 4-(b) and 4-(d) are swept counterclockwise and are characterized by points with a vertical tangent, representing the maximum value of  $-\bar{s}_r$ , namely the maximum temporal damping for the propagating wave.

To conclude the study of temporal damping, a parametric analysis has been conducted to investigate the influence of the TPMS wall thickness on the frequency response of the viscoelastic structure. This study aims to highlight the role of thickness as a geometrical parameter in shaping the dynamic behavior of the system. The Fig. 5 represents the spectral properties of a TPMS-based structure where the scalar field  $f(\mathbf{x})$  of equation (52) satisfies  $f_1 \leq f(\mathbf{x}) \leq f_2$  with  $f_1 = 0.2$  and  $f_2 = 0.7$ . All the other features are maintained identical to the case of Fig. 2. As can be observed, the increase in thickness of the TPMS layer leads to an increase in the system's stiffness, which outweighs the increase in mass.

This results, on one hand, in higher values of  $\bar{s}_i$  and, on the other hand, in lower values of  $\bar{s}_r$  with respect the case of the thinner TPMS layer of Fig: 2. The decrease of  $\bar{s}_r$  is associated with reduced viscous dissipation, as also confirmed by the representations in Fig. 5-(b), (c), and (d), which is also due to the reduced amount of epoxy material in the periodic cell.

When the spatial damping is investigated, the complex-valued wave vector  $\mathbf{k}$  plays the role of the eigenvalue of the algebraic eigenproblem (35), while  $s = i\omega$  with  $\omega \in \mathbb{R}$  is a parameter. The Fig. 6 shows the obtained spectrum in the case of one single term in the Prony series (1) with relaxation time  $\tau_r^1 \omega_{ref} = 10^{-2}$ . To complement the set of numerical examples presented, an additional case study is considered in which the viscoelastic behavior of the epoxy material is modeled using a Prony series with six relaxation terms. This choice reflects a more detailed characterization of the time-dependent mechanical response, as commonly adopted for polymeric materials [2, 34, 88, 89]. The values adopted for the relaxation times and the viscosity ratios are

$$\begin{aligned} \tau_r^1 \omega_{ref} &= 0.5072, & \gamma^1 &= 0.11070, \\ \tau_r^2 \omega_{ref} &= 2.8798, & \gamma^2 &= 0.13170, \\ \tau_r^3 \omega_{ref} &= 16.3450, & \gamma^3 &= 0.151875, \\ \tau_r^4 \omega_{ref} &= 92.7856, & \gamma^4 &= 0.133125, \\ \tau_r^5 \omega_{ref} &= 526.5938, & \gamma^5 &= 0.051015, \\ \tau_r^6 \omega_{ref} &= 2.9902 \cdot 10^3, & \gamma^6 &= 0.008542, \end{aligned} \tag{53}$$

according to [2] and the relative spectra are plotted in Fig. 7. In particular, setting  $\mathbf{n} = \mathbf{e}_1$ , the dimensionless components  $\bar{k}_{1r}$  and  $\bar{k}_{1i}$  of  $\bar{k}_1 = k_1 d$  are represented in terms of  $\bar{\omega} = \omega / \omega_{ref}$  in a selected range, spanning from 0 to 0.3. The spectra describe the band structure of the considered periodic material, with pass bands corresponding to progressive and regressive propagating waves associated with non-zero values of  $\bar{k}_{1r}$  and band gaps, describing spatial wave attenuation phenomena associated to non-zero values of  $\bar{k}_{1i}$ . Expressing with  $\lambda = \exp(ik_1 d)$  the Floquet multiplier, Figs 6-(b) and 7-(b) show its real and imaginary components in terms of  $\bar{\omega}$ . As expected, the curves wrap around the unitary cylinder as  $\bar{\omega}$  increases, escaping from that in correspondence with those  $\bar{\omega}$  values in which dissipation occurs. Magenta curve in Figs 6 and 7 represent the results obtained from a first order asymptotic/variational-asymptotic homogenization technique developed in [17, 21] for viscoelastic materials. As expected, the homogenized model accurately reproduce the spectral behaviour of the material in the long wavelength regime and at low frequencies.

Finally, the accuracy of the proposed model is further successfully validated in Appendix E. The Floquet–Bloch spectrum obtained using the model for a cubic periodic cell containing an inclusion of the same shape is compared with the results provided by the commercial finite element software *COMSOL Multiphysics*®.

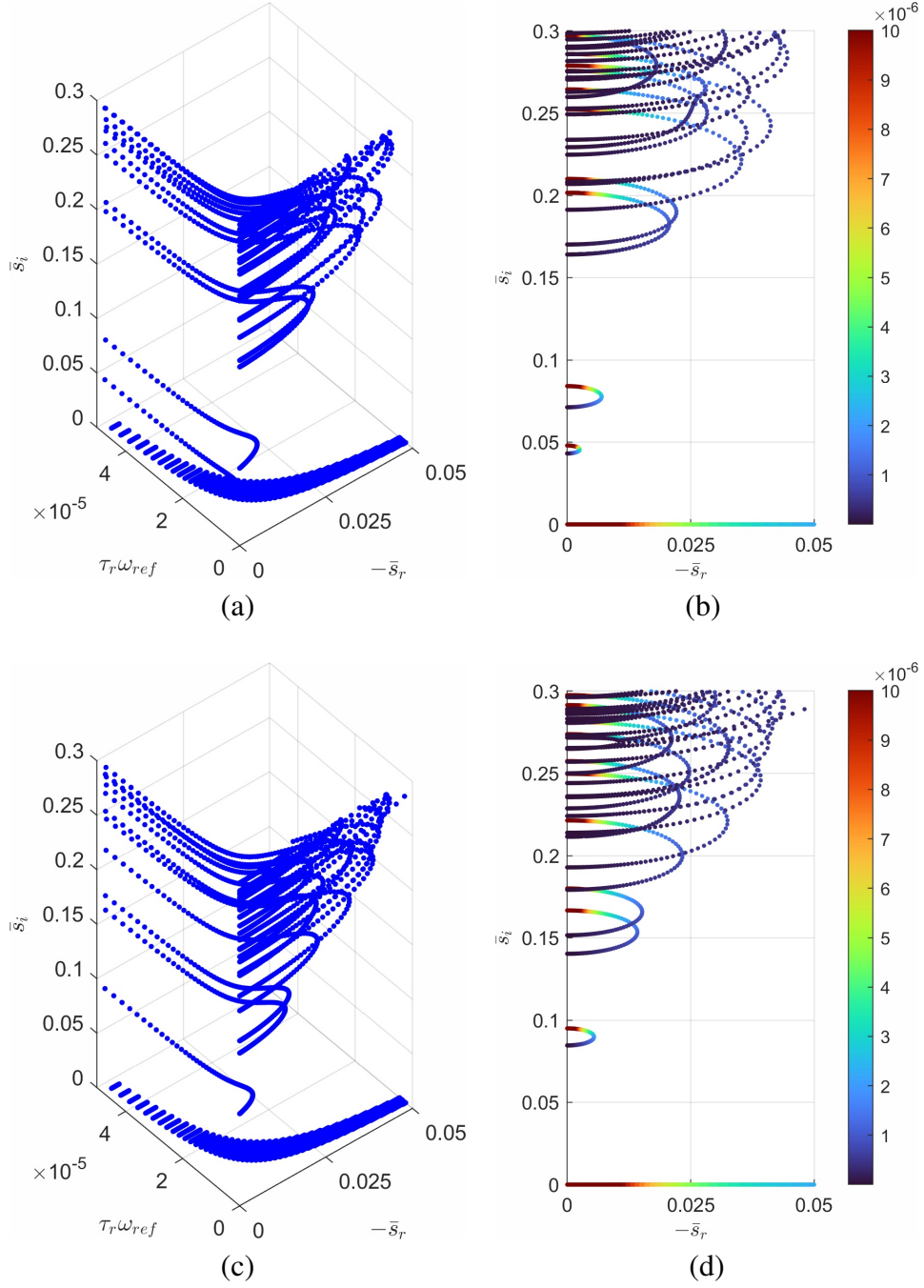


Figure 4: Real and imaginary components of  $\bar{s} = s/\omega_{ref}$  in terms of dimensionless relaxation time  $\tau\omega_{ref}$  with  $\omega_{ref} = \sqrt{\frac{E}{\rho}} \frac{1}{d}$  evaluated with respect to the steel phase for the case  $N=1$  and  $k_1d = \pi/3$  (a) and (b) and for  $k_1d = 2\pi/3$  (c) and (d). Three-dimensional representations (a) and (c) and two-dimensional ones parametrized for  $\tau\omega_{ref}$  (b) and (d).

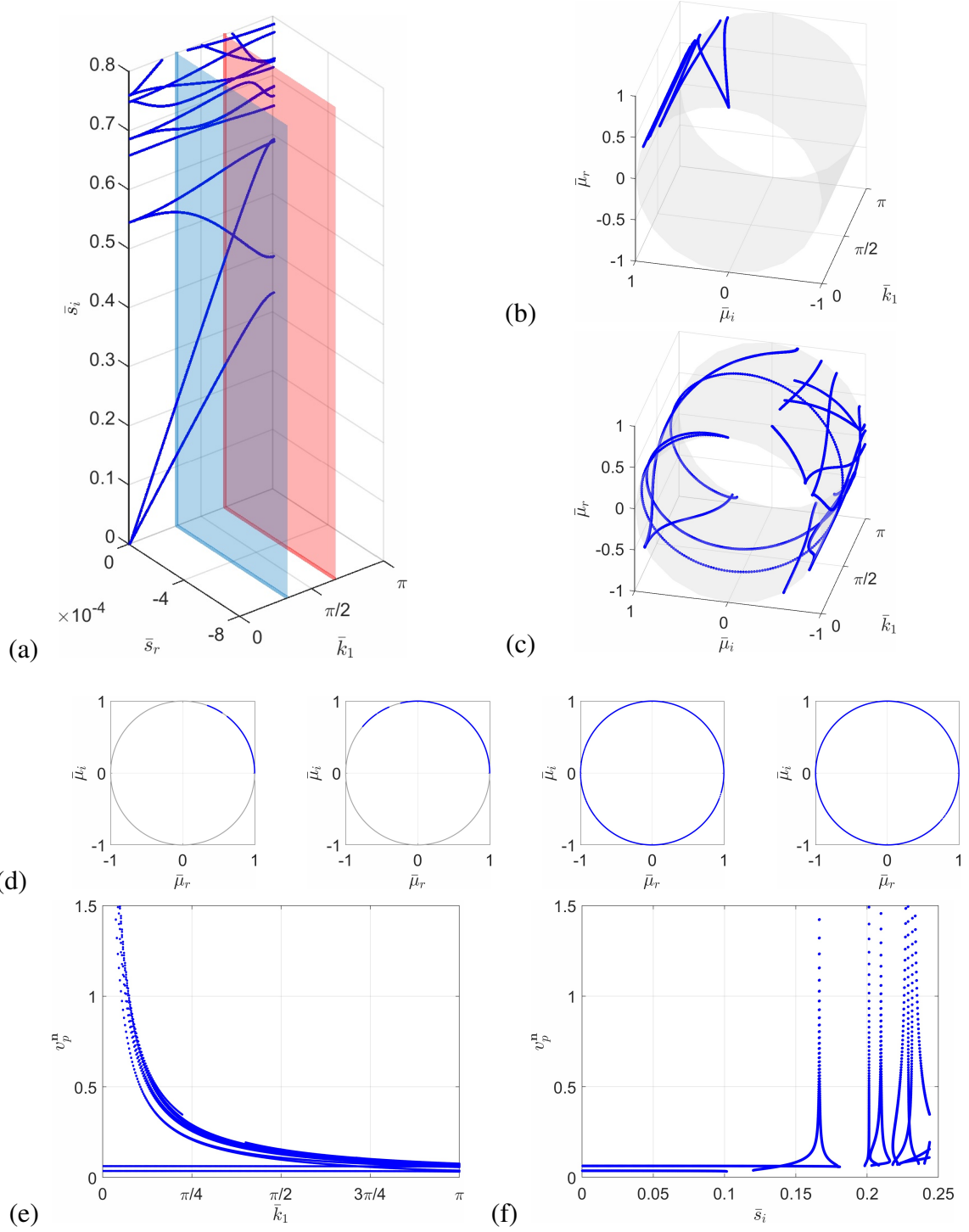


Figure 5: Analysis of temporal damping in the case of  $N=1$  with relaxation time  $\tau_r^1 \omega_{ref} = 10^{-5}$  and  $\omega_{ref} = d^{-1} \sqrt{\frac{E}{\rho}}$ , evaluated with respect to the steel phase. Thicker TPMS layer with respect to the case of Fig. 2. (a) Full three-dimensional representation of the complex dispersion curves for waves propagating along  $\mathbf{n} = \mathbf{e}_1$ . (b) Dispersion curves plotted on the unit cylindrical surface in terms of the real part of the normalized frequency  $\bar{\mu}$  for dimensionless time  $\bar{\tau} = t \omega_{ref} = 5$ . (c) Same as (b) but for  $\bar{\tau} = 50$ . (d) Comparison of dispersion curves on the unit circle for different dimensionless times  $\bar{\tau} = 5, 10, 50, 100$ , showing the effect of increasing viscous dissipation. (e) Magnitude of the phase velocity  $v_p^n$  as a function of the normalized wavenumber  $\bar{k}_1$ . (f) Same quantity plotted with respect to the imaginary part of the complex frequency  $\bar{s}_i$ .

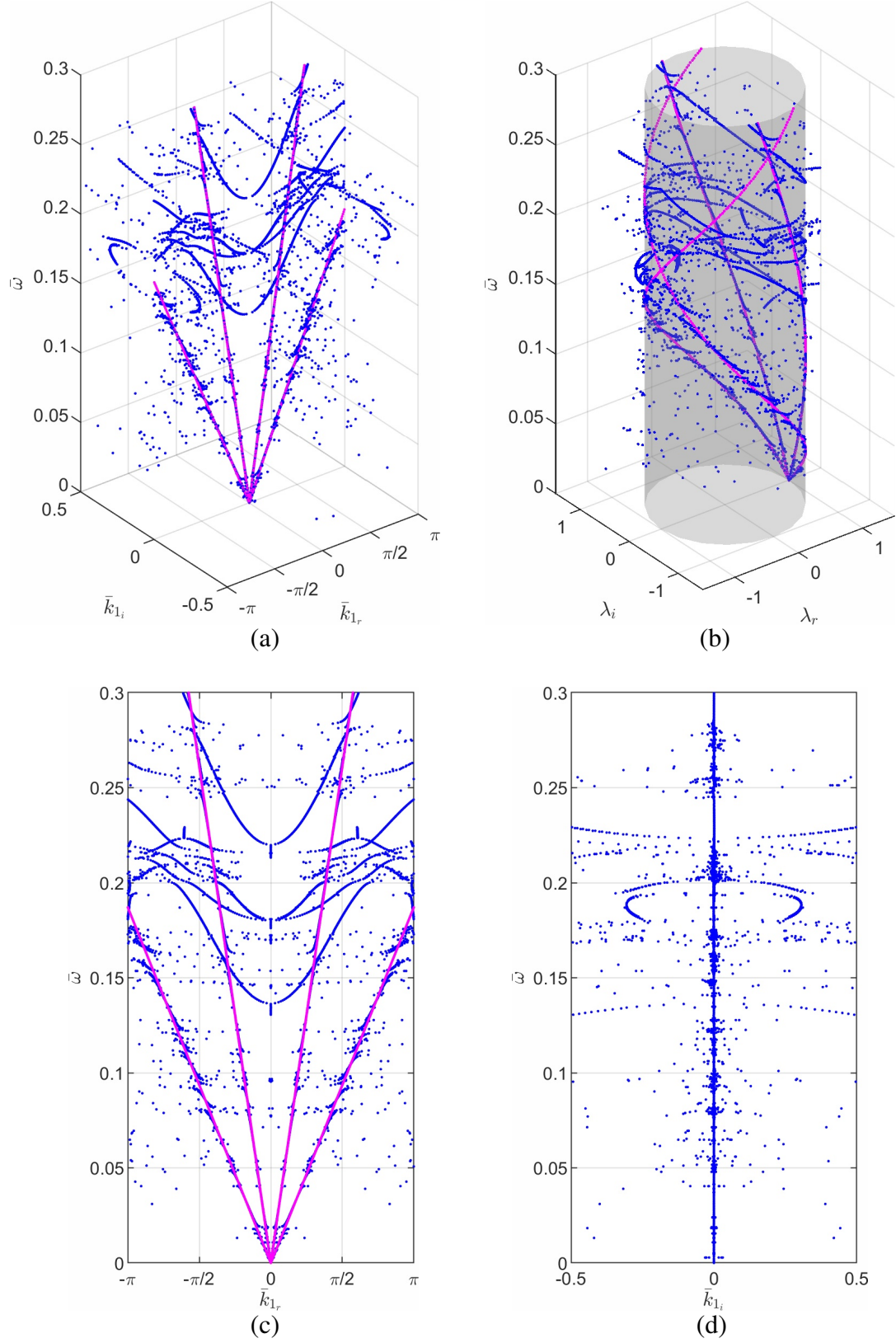


Figure 6: Spatial damping and one relaxation time  $\tau_r^1 \omega_{ref} = 10^{-5}$  with  $\omega_{ref} = \frac{1}{d} \sqrt{\frac{E}{\rho}}$  evaluated with respect to the steel phase. Three-dimensional spectrum (a), real and imaginary components of Floquet multiplier  $\lambda = \exp(ik_1 d)$  (b), two-dimensional spectrum in the plane  $(\bar{k}_{1r} - \bar{\omega})$  (c), two-dimensional spectrum in the plane  $(\bar{k}_{1i} - \bar{\omega})$  (d). Magenta curves refer to the first-order homogenized model [17, 21].

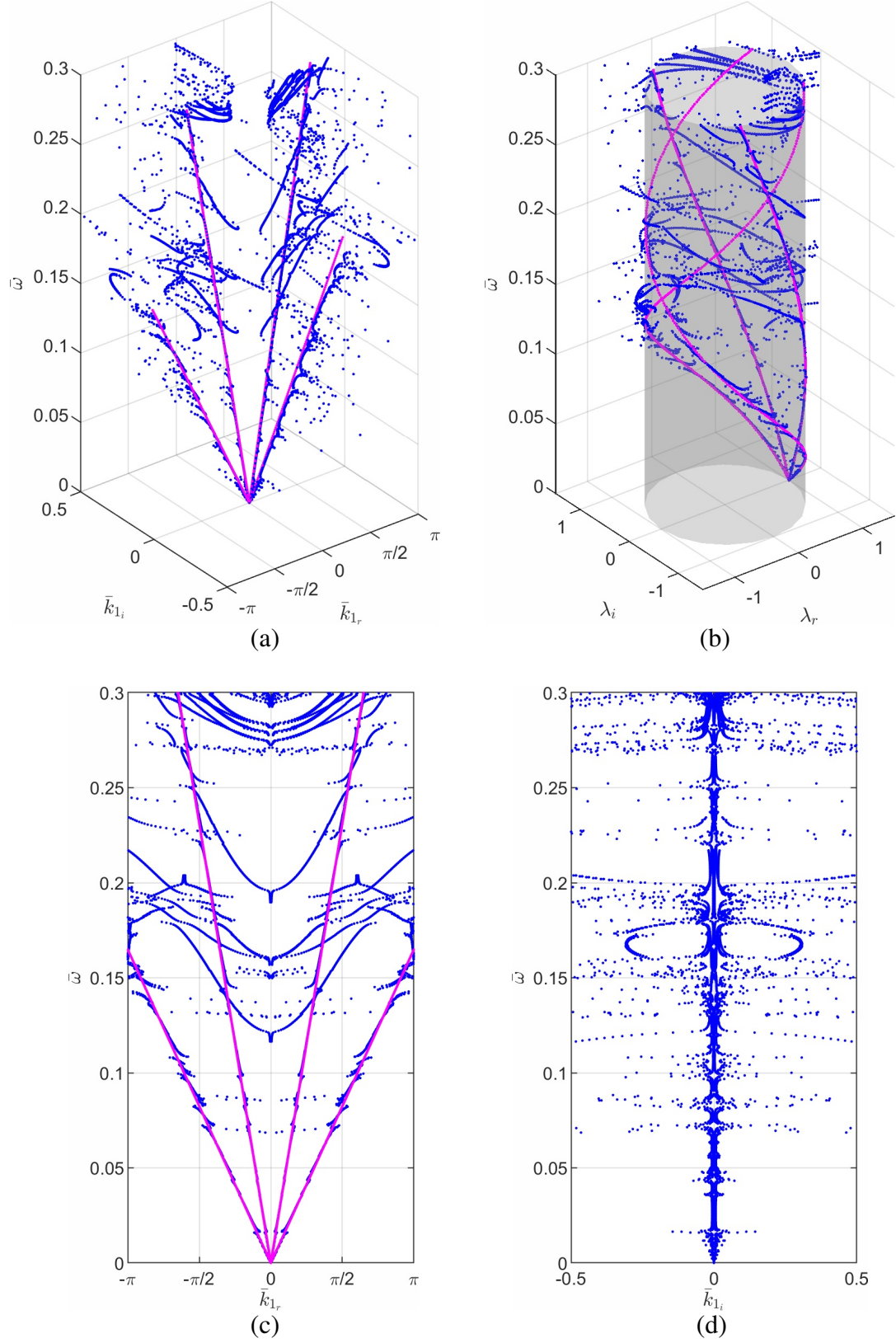


Figure 7: Spatial damping and six relaxation times (see eq.(53)). Three-dimensional spectrum (a), real and imaginary components of Floquet multiplier  $\lambda = \exp(ik_1d)$  (b), two-dimensional spectrum in the plane  $(\bar{k}_{1r} - \bar{\omega})$  (c), two-dimensional spectrum in the plane  $(\bar{k}_{1i} - \bar{\omega})$  (d). Magenta curves refer to the first-order homogenized model [17, 21].



## 7. Final remarks and future developments

This study introduces a comprehensive framework for analysing wave propagation in viscoelastic architected metamaterials with complex three-dimensional topologies, focusing on their dispersion properties governed by damped Bloch waves. Fourier-based techniques were employed to efficiently solve the governing dynamic equations, while quasi-Monte Carlo integration allowed for accurate computation of the Fourier coefficients, even in the presence of highly intricate geometries.

The enhanced derationalization technique proved particularly effective in handling rational eigenvalue problems associated with temporal damping, demonstrating its capability to handle even large-scale systems. The methodology enables the computation of the Floquet-Bloch spectrum in both cases of complex frequency parameterised by real wave number (temporal damping) and the complementary scenario of complex wave number parameterised by real frequency (spatial damping), thus offering a unified approach to characterise wave attenuation in dissipative periodic media. The rational eigenvalue problems associated with temporal damping are particularly challenging to solve using conventional numerical techniques, which further emphasizes the practical utility of the proposed methodology, especially in the context of vibration attenuation and noise reduction applications.

The proposed framework has been applied to a set of representative case studies, including a TPMS-based viscoelastic metamaterial. The results highlight how the introduction of the viscoelastic phase alters the dispersion properties. In particular, the band structure is strongly influenced by the relaxation behaviour and by the number of terms retained in the Prony series, revealing a non-monotonic dependence on the relaxation times. A preliminary analysis with varying thicknesses of the TPMS suggests that this parameter can influence the dispersion response, indicating the relevance of accounting for it in the design of the metamaterials.

Future research will aim to enhance the computational efficiency of qMC integration by exploring compression techniques, such as the Tchakaloff-Davis-Wilhelmsen method, to reduce the number of required points. Additionally, strategies to mitigate spectral noise in eigenvalue problems, including the use of Gibbs filters or improved noise suppression methods, will be investigated. These improvements, while potentially increasing computational times, could further refine the precision of the results.

## Acknowledgments

F. Fantoni, M.L. De Bellis and A. Bacigalupo are members of INdAM-GNFM. The authors gratefully acknowledge the National Group of Mathematical Physics (GNFM-INdAM, Italy), the financial support of the European Union – Next Generation EU, under the call PRIN 2022 of the Italian Minister of University and Research (MUR) - Project 202222LB37 (PE: Physical Sciences and Engineering): “Advanced Design of avant-garde ACTIVE microstructured materials via additive manufacturing (ADACTIVE)”. This research has been also accomplished within Rete Italiana di Approssimazione (RITA), the thematic group on “Teoria dell’Approssimazione e Applicazioni” (TAA) of the Italian Mathematical Union and with the support of GNCS-INdAM.

## Appendix A: infinite-dimensional algebraic operators involved in Equation (19)

The operators  $\mathbf{A}$ ,  $\mathbf{B}$  and  $\mathbf{C}_{ijh\ell}$  involved in Equation (19) are detailed in what follows. The first operator  $\mathbf{A} : \ell_2(\mathbb{Z}^3)^3 \rightarrow \ell_2(\mathbb{Z}^3)^3$  is hence detailed in each of its infinite part as

$$\begin{aligned} \mathbf{A}[\text{col}(\mathbf{u}_1, \mathbf{u}_2, \mathbf{u}_3)]^{m^1} = \sum_{n \in \mathbb{Z}^3} & \left( -((m_r - n_r)p_j^r)(n_s p_\ell^s)[C_{1jh\ell}^{\mathfrak{A} \setminus \mathfrak{C}}]_{m-n}[\tilde{u}_h]_n - (n_r p_j^r)(n_s p_\ell^s)[C_{1jh\ell}^{\mathfrak{A} \setminus \mathfrak{C}}]_{m-n}[\tilde{u}_h]_n + \right. \\ & + (n_r p_j^r)k_\ell[C_{1jh\ell}^{\mathfrak{A} \setminus \mathfrak{C}}]_{m-n}[\tilde{u}_h]_n + (n_r p_j^r)k_\ell[C_{1\ell h j}^{\mathfrak{A} \setminus \mathfrak{C}}]_{m-n}[\tilde{u}_h]_n + \\ & \left. + ((m_r - n_r)p_j^r)k_\ell[C_{1jh\ell}^{\mathfrak{A} \setminus \mathfrak{C}}]_{m-n}[\tilde{u}_h]_n - k_j k_\ell[C_{1jh\ell}^{\mathfrak{A} \setminus \mathfrak{C}}]_{m-n}[\tilde{u}_h]_n \right), \end{aligned} \quad (54a)$$

$$\begin{aligned} \mathbf{A}[\text{col}(\mathbf{u}_1, \mathbf{u}_2, \mathbf{u}_3)]^{m^2} = \sum_{n \in \mathbb{Z}^3} & \left( -((m_r - n_r)p_j^r)(n_s p_\ell^s)[C_{2jh\ell}^{\mathfrak{A} \setminus \mathfrak{C}}]_{m-n}[\tilde{u}_h]_n - (n_r p_j^r)(n_s p_\ell^s)[C_{2jh\ell}^{\mathfrak{A} \setminus \mathfrak{C}}]_{m-n}[\tilde{u}_h]_n + \right. \\ & + (n_r p_j^r)k_\ell[C_{2jh\ell}^{\mathfrak{A} \setminus \mathfrak{C}}]_{m-n}[\tilde{u}_h]_n + (n_r p_j^r)k_\ell[C_{2\ell h j}^{\mathfrak{A} \setminus \mathfrak{C}}]_{m-n}[\tilde{u}_h]_n + \\ & \left. + ((m_r - n_r)p_j^r)k_\ell[C_{2jh\ell}^{\mathfrak{A} \setminus \mathfrak{C}}]_{m-n}[\tilde{u}_h]_n - k_j k_\ell[C_{2jh\ell}^{\mathfrak{A} \setminus \mathfrak{C}}]_{m-n}[\tilde{u}_h]_n \right), \end{aligned} \quad (54b)$$

$$\begin{aligned} \mathbf{A}[\text{col}(\mathbf{u}_1, \mathbf{u}_2, \mathbf{u}_3)]^{m^3} = \sum_{n \in \mathbb{Z}^3} & \left( -((m_r - n_r)p_j^r)(n_s p_\ell^s)[C_{3jh\ell}^{\mathfrak{A} \setminus \mathfrak{C}}]_{m-n}[\tilde{u}_h]_n - (n_r p_j^r)(n_s p_\ell^s)[C_{3jh\ell}^{\mathfrak{A} \setminus \mathfrak{C}}]_{m-n}[\tilde{u}_h]_n + \right. \\ & + (n_r p_j^r)k_\ell[C_{3jh\ell}^{\mathfrak{A} \setminus \mathfrak{C}}]_{m-n}[\tilde{u}_h]_n + (n_r p_j^r)k_\ell[C_{3\ell h j}^{\mathfrak{A} \setminus \mathfrak{C}}]_{m-n}[\tilde{u}_h]_n + \\ & \left. + ((m_r - n_r)p_j^r)k_\ell[C_{3jh\ell}^{\mathfrak{A} \setminus \mathfrak{C}}]_{m-n}[\tilde{u}_h]_n - k_j k_\ell[C_{3jh\ell}^{\mathfrak{A} \setminus \mathfrak{C}}]_{m-n}[\tilde{u}_h]_n \right), \end{aligned} \quad (54c)$$

the second operator  $\mathbf{B} : \ell_2(\mathbb{Z}^3)^3 \rightarrow \ell_2(\mathbb{Z}^3)^3$  is given by

$$\mathbf{B}[\text{col}(\mathbf{u}_1, \mathbf{u}_2, \mathbf{u}_3)]^{m^1} = - \sum_{n \in \mathbb{Z}^3} [\rho]_{m-n}[\tilde{u}_1]_n, \quad (55a)$$

$$\mathbf{B}[\text{col}(\mathbf{u}_1, \mathbf{u}_2, \mathbf{u}_3)]^{m^2} = - \sum_{n \in \mathbb{Z}^3} [\rho]_{m-n}[\tilde{u}_2]_n, \quad (55b)$$

$$\mathbf{B}[\text{col}(\mathbf{u}_1, \mathbf{u}_2, \mathbf{u}_3)]^{m^3} = - \sum_{n \in \mathbb{Z}^3} [\rho]_{m-n}[\tilde{u}_3]_n, \quad (55c)$$

and the remaining operators  $\mathbf{C}_{1jh\ell}, \mathbf{C}_{2jh\ell}, \mathbf{C}_{3jh\ell} : \ell_2(\mathbb{Z}^3)^3 \rightarrow \ell_2(\mathbb{Z}^3)^3$  are defined as

$$\begin{aligned} \mathbf{C}_{1jh\ell}[\text{col}(\mathbf{u}_1, \mathbf{u}_2, \mathbf{u}_3)]^{m^1} = \sum_{n \in \mathbb{Z}^2} & -((m_r - n_r)p_j^r)(n_s p_\ell^s)[\chi_\mathfrak{C}]_{m-n}[\tilde{u}_h]_n - k_j k_\ell[\chi_\mathfrak{C}]_{m-n}[\tilde{u}_h]_n + \\ & - (n_r p_j^r)(n_s p_\ell^s)[\chi_\mathfrak{C}]_{m-n}[\tilde{u}_h]_n + (n_r p_j^r)k_\ell[\chi_\mathfrak{C}]_{m-n}[\tilde{u}_h]_n + \\ & + (n_r p_\ell^r)k_j[\chi_\mathfrak{C}]_{m-n}[\tilde{u}_h]_n + ((m_r - n_r)p_j^r)k_\ell[\chi_\mathfrak{C}]_{m-n}[\tilde{u}_h]_n, \end{aligned} \quad (56a)$$

$$\mathbf{C}_{1jh\ell}[\text{col}(\mathbf{u}_1, \mathbf{u}_2, \mathbf{u}_3)]^{m^2} = 0, \quad (56b)$$

$$\mathbf{C}_{1jh\ell}[\text{col}(\mathbf{u}_1, \mathbf{u}_2, \mathbf{u}_3)]^{m^3} = 0, \quad (56c)$$

$$\mathbf{C}_{2jh\ell}[\text{col}(\mathbf{u}_1, \mathbf{u}_2, \mathbf{u}_3)]^{m^1} = 0, \quad (56d)$$



$$\begin{aligned}
C_{2jhl}[\text{col}(\mathbf{u}_1, \mathbf{u}_2, \mathbf{u}_3)]^{m^2} &= \sum_{n \in \mathbb{Z}^2} -((m_r - n_r)p_j^r)(n_s p_\ell^s)[\chi_{\mathfrak{C}}]_{m-n}[\tilde{u}_h]_n - k_j k_\ell [\chi_{\mathfrak{C}}]_{m-n}[\tilde{u}_h]_n + \\
&\quad - (n_r p_j^r)(n_s p_\ell^s)[\chi_{\mathfrak{C}}]_{m-n}[\tilde{u}_h]_n + (n_r p_j^r)k_\ell [\chi_{\mathfrak{C}}]_{m-n}[\tilde{u}_h]_n + \\
&\quad + (n_r p_\ell^r)k_j [\chi_{\mathfrak{C}}]_{m-n}[\tilde{u}_h]_n + ((m_r - n_r)p_j^r)k_\ell [\chi_{\mathfrak{C}}]_{m-n}[\tilde{u}_h]_n.
\end{aligned} \tag{56e}$$

$$C_{2jhl}[\text{col}(\mathbf{u}_1, \mathbf{u}_2, \mathbf{u}_3)]^{m^3} = 0, \tag{56f}$$

$$C_{3jhl}[\text{col}(\mathbf{u}_1, \mathbf{u}_2, \mathbf{u}_3)]^{m^1} = 0, \tag{56g}$$

$$C_{3jhl}[\text{col}(\mathbf{u}_1, \mathbf{u}_2, \mathbf{u}_3)]^{m^3} = 0, \tag{56h}$$

$$\begin{aligned}
C_{3jhl}[\text{col}(\mathbf{u}_1, \mathbf{u}_2, \mathbf{u}_3)]^{m^2} &= \sum_{n \in \mathbb{Z}^2} -((m_r - n_r)p_j^r)(n_s p_\ell^s)[\chi_{\mathfrak{C}}]_{m-n}[\tilde{u}_h]_n - k_j k_\ell [\chi_{\mathfrak{C}}]_{m-n}[\tilde{u}_h]_n + \\
&\quad - (n_r p_j^r)(n_s p_\ell^s)[\chi_{\mathfrak{C}}]_{m-n}[\tilde{u}_h]_n + (n_r p_j^r)k_\ell [\chi_{\mathfrak{C}}]_{m-n}[\tilde{u}_h]_n + \\
&\quad + (n_r p_\ell^r)k_j [\chi_{\mathfrak{C}}]_{m-n}[\tilde{u}_h]_n + ((m_r - n_r)p_j^r)k_\ell [\chi_{\mathfrak{C}}]_{m-n}[\tilde{u}_h]_n.
\end{aligned} \tag{56i}$$

## Appendix B: infinite-dimensional algebraic operators involved in Equation (33)

The infinite-dimensional algebraic operators  $\mathbf{A}^{(k)}$ ,  $\mathbf{B}^{(k)}$ , and  $\mathbf{C}^{(k)}$  involved in Equation (33) are detailed in what follows. The first operator  $\mathbf{A}^{(k)} : \ell_2(\mathbb{Z}^3)^3 \rightarrow \ell_2(\mathbb{Z}^3)^3$  is defined as

$$\begin{aligned}
\mathbf{A}^{(k)}[\text{col}(\mathbf{u}_1, \mathbf{u}_2, \mathbf{u}_3)]^{m^1} &= \sum_{n \in \mathbb{Z}^3} -((m_r - n_r)p_j^r)(n_s p_\ell^s)[\hat{C}_{1jhl}]_{m-n}[\tilde{u}_h]_n - (n_r p_j^r)(n_s p_\ell^s)[\hat{C}_{1jhl}]_{m-n} \\
&\quad - [\rho]_{m-n} s^2 [\tilde{u}_1]_n
\end{aligned} \tag{57a}$$

$$\begin{aligned}
\mathbf{A}^{(k)}[\text{col}(\mathbf{u}_1, \mathbf{u}_2, \mathbf{u}_3)]^{m^2} &= \sum_{n \in \mathbb{Z}^3} -((m_r - n_r)p_j^r)(n_s p_\ell^s)[\hat{C}_{2jhl}]_{m-n}[\tilde{u}_h]_n - (n_r p_j^r)(n_s p_\ell^s)[\hat{C}_{2jhl}]_{m-n} \\
&\quad - [\rho]_{m-n} s^2 [\tilde{u}_2]_n
\end{aligned} \tag{57b}$$

$$\begin{aligned}
\mathbf{A}^{(k)}[\text{col}(\mathbf{u}_1, \mathbf{u}_2, \mathbf{u}_3)]^{m^3} &= \sum_{n \in \mathbb{Z}^3} -((m_r - n_r)p_j^r)(n_s p_\ell^s)[\hat{C}_{3jhl}]_{m-n}[\tilde{u}_h]_n - (n_r p_j^r)(n_s p_\ell^s)[\hat{C}_{3jhl}]_{m-n} \\
&\quad - [\rho]_{m-n} s^2 [\tilde{u}_3]_n.
\end{aligned} \tag{57c}$$

The second operator  $\mathbf{B}^{(k)} : \ell_2(\mathbb{Z}^3)^3 \rightarrow \ell_2(\mathbb{Z}^3)^3$  is

$$\begin{aligned}
\mathbf{B}^{(k)}[\text{col}(\mathbf{u}_1, \mathbf{u}_2, \mathbf{u}_3)]^{m^1} &= \sum_{n \in \mathbb{Z}^3} (n_r p_j^r) \kappa_\ell [\hat{C}_{1jhl}]_{m-n}[\tilde{u}_h]_n + (n_r p_j^r) \kappa_\ell [\hat{C}_{1\ell hj}]_{m-n}[\tilde{u}_h]_n \\
&\quad + ((m_r - n_r)p_j^r) \kappa_\ell [\hat{C}_{1jhl}]_{m-n}[\tilde{u}_h]_n
\end{aligned} \tag{58a}$$

$$\begin{aligned}
\mathbf{B}^{(k)}[\text{col}(\mathbf{u}_1, \mathbf{u}_2, \mathbf{u}_3)]^{m^2} &= \sum_{n \in \mathbb{Z}^3} (n_r p_j^r) \kappa_\ell [\hat{C}_{2jhl}]_{m-n}[\tilde{u}_h]_n + (n_r p_j^r) \kappa_\ell [\hat{C}_{2\ell hj}]_{m-n}[\tilde{u}_h]_n \\
&\quad + ((m_r - n_r)p_j^r) \kappa_\ell [\hat{C}_{2jhl}]_{m-n}[\tilde{u}_h]_n
\end{aligned} \tag{58b}$$

$$\begin{aligned}
B^{(k)}[\text{col}(\mathbf{u}_1, \mathbf{u}_2, \mathbf{u}_3)]^{m^3} &= \sum_{n \in \mathbb{Z}^3} (n_r p_j^r) \kappa_\ell [\hat{C}_{3jh\ell}]_{m-n} [\tilde{u}_h]_n + (n_r p_j^r) \kappa_\ell [\hat{C}_{3\ell hj}]_{m-n} [\tilde{u}_h]_n \\
&\quad + ((m_r - n_r) p_j^r) \kappa_\ell [\hat{C}_{3j h \ell}]_{m-n} [\tilde{u}_h]_n.
\end{aligned} \tag{58c}$$

Lastly, the third  $C^{(k)} : \ell_2(\mathbb{Z}^3)^3 \rightarrow \ell_2(\mathbb{Z}^3)^3$  is

$$C^{(k)}[\text{col}(\mathbf{u}_1, \mathbf{u}_2, \mathbf{u}_3)]^{m^1} = \sum_{n \in \mathbb{Z}^3} -\kappa_j \kappa_\ell [\hat{C}_{1jh\ell}]_{m-n} [\tilde{u}_h]_n \tag{59a}$$

$$C^{(k)}[\text{col}(\mathbf{u}_1, \mathbf{u}_2, \mathbf{u}_3)]^{m^2} = \sum_{n \in \mathbb{Z}^3} -\kappa_j \kappa_\ell [\hat{C}_{2jh\ell}]_{m-n} [\tilde{u}_h]_n \tag{59b}$$

$$C^{(k)}[\text{col}(\mathbf{u}_1, \mathbf{u}_2, \mathbf{u}_3)]^{m^3} = \sum_{n \in \mathbb{Z}^3} -\kappa_j \kappa_\ell [\hat{C}_{3jh\ell}]_{m-n} [\tilde{u}_h]_n. \tag{59c}$$

### Appendix C: modicum of the construction of Sobol sequences for qMC integration

Sequences that are nets provide a method to obtain well-distributed points in the periodic cube, which are suitable for quasi-Monte Carlo (qMC) integration. The concept of  $(t, m, d)$ -nets involves subdividing the cube into smaller intervals and placing points such that each of these intervals contains a prescribed number of points. For this reason, the following two definitions are important.

**Definition A.1.** Let  $t \geq 0$ ,  $m \geq 1$ ,  $d \geq 1$ , and  $b \geq 2$  be integers with  $t \leq m$ . A  $(t, m, d)$ -net in base  $b$  is a point set  $P$  consisting in  $b^m$  points in  $[0, 1)^d$  such that every elementary interval of the form

$$\prod_{j=1}^d \left[ \frac{a_j}{b^{e_j}}, \frac{a_j + 1}{b^{e_j}} \right), \tag{60}$$

with each  $e_j \geq 0$ ,  $0 \leq a_j < b^{e_j}$ , and  $e_1 + e_2 + \dots + e_d = m - t$ , contains exactly  $b^t$  points of  $P$ .

**Definition A.2.** Let  $t \geq 0$  and  $d \geq 1$  be integers. A  $(t, d)$ -sequence in base  $b$  is a sequence of points  $S = \{\mathbf{x}_0, \mathbf{x}_1, \dots\}$  in  $[0, 1)^d$  such that for any integers  $m > t$  and  $\ell \geq 0$ , every block of  $b^m$  points, that is  $\mathbf{x}_{\ell b^m}, \dots, \mathbf{x}_{(\ell+1)b^m-1}$  in  $S$  forms a  $(t, m, d)$ -net in base  $b$ .

Sobol sequences, which were used in the numerical experiments, represent the first known construction of  $(t, d)$ -sequences [90]. These sequences are generated through the digital construction scheme (see, e.g., [54]).

Let  $b$  be a prime number, and let  $\mathbb{Z}_b := \{0, 1, \dots, b-1\}$  denote the set of equivalence classes of integers modulo  $b$ . When endowed with addition and multiplication,  $\mathbb{Z}_b$  forms a finite field of order  $b$ . Consider  $C_1, \dots, C_d$  to be  $m \times m$  matrices with entries in  $\mathbb{Z}_b$ . The  $j$ -th component of the  $i$ -th point in a sequence  $P = \{\mathbf{t}_0, \dots, \mathbf{t}_{b^m-1}\}$  is constructed by first expressing  $i$  in base  $b$ :

$$i = (i_m \dots i_2 i_1)_b = i_1 + i_2 b + \dots + i_m b^{m-1}. \tag{61}$$

Next, the product of  $C_j$  and the base- $b$  representation of  $i$  is computed, with all operations performed in the field  $\mathbb{Z}_b$ :

$$\begin{pmatrix} y_1 \\ y_2 \\ \vdots \\ y_m \end{pmatrix} = C_j \begin{pmatrix} i_1 \\ i_2 \\ \vdots \\ i_m \end{pmatrix}. \quad (62)$$

The  $j$ -th component of the  $i$ -th point,  $t_{i,j}$ , is then defined as

$$t_{i,j} = (0.y_1y_2 \cdots y_m)_b = \frac{y_1}{b} + \frac{y_2}{b^2} + \cdots + \frac{y_m}{b^m}. \quad (63)$$

The resulting points are known as digital nets over  $\mathbb{Z}_b$ . When  $(t, m, d)$ -nets or  $(t, d)$ -sequences are constructed over  $\mathbb{Z}_b$ , they are referred to as digital  $(t, m, d)$ -nets or digital  $(t, d)$ -sequences over  $\mathbb{Z}_b$ , respectively. In particular, Sobol sequences are digital  $(t, d)$ -sequences over  $\mathbb{Z}_2$ . In such cases, the matrices  $C_j$  are generated using primitive polynomials (see, e.g., [52, p. 266]). Let  $p_1, \dots, p_d \in \mathbb{Z}_2[x]$  be distinct primitive polynomials ordered by degree. Each polynomial can be written as

$$p_j(x) = x^{e_j} + a_{1,j}x^{e_j-1} + \cdots + a_{e_j-1,j}x + 1, \quad \text{for } 1 \leq j \leq d, \quad (64)$$

where  $a_{k,j} \in \mathbb{Z}_2$ . A sequence of  $e_j$  odd integers  $1 \leq m_{1,j}, \dots, m_{e_j,j}$  is then selected such that  $m_{k,j} < 2^k$  for  $1 \leq k \leq e_j$ . For  $k > e_j$ , the values  $m_{k,j}$  are defined recursively as follows:

$$m_{k,j} = 2a_{1,j}m_{k-1,j} \oplus \cdots \oplus 2^{e_j-1}a_{e_j-1,j}m_{k-e_j+1,j} \oplus 2^{e_j}m_{k-e_j,j} \oplus m_{k-e_j,j}, \quad (65)$$

where  $\oplus$  denotes the bitwise exclusive-or operator. From this construction, the so-called direction numbers are obtained as

$$v_{k,j} = \frac{m_{k,j}}{2^k}, \quad (66)$$

which are then used to compute the elements  $t_{i,j}$ , where

$$t_{i,j} = i_0v_{1,j} \oplus i_1v_{2,j} \oplus \cdots \oplus i_{r-1}v_{r,j}, \quad (67)$$

and  $i = (i_{r-1} \cdots i_1 i_0)_2$  is the binary representation of  $i$ . As a result of this construction, it can be shown that Sobol sequences are digital  $(t, d)$ -sequences with  $t = \sum_{j=1}^d (e_j - 1)$ .

#### Appendix D: approximation of Fourier coefficients via qMC integration

In the present appendix, a brief analysis is provided concerning the quasi-Monte Carlo (qMC) approximation introduced in Section 5. In particular, attention is devoted to Proposition 5.2, by analyzing the relative error between the exact analytical computation of the test-case coefficients and their corresponding qMC approximations.

In this simplified test, the Fourier coefficients of a periodic cell such as the one shown in Fig. 8 are considered. The periodic cell, as in the previous tests, is a cube of size  $d = 10^{-2}$  m. The exterior matrix consists of epoxy, while the inner cube—centered within the cell and having an edge length of  $\ell_C = 0.4 \cdot 10^{-2}$  m—is composed of steel. In this case, the Fourier coefficients can be computed analytically by exploiting the linearity of the integral, since the tensor components and the mass density are piecewise constant within the respective subdomains. Therefore, the integrand can be treated as a

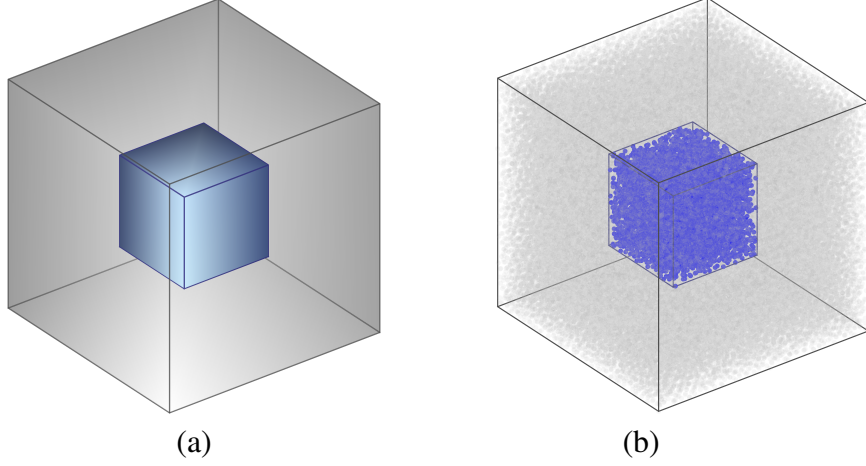


Figure 8: Visualization of the periodic cell used in the quasi-Monte Carlo analysis. (a) Geometric model of the periodic cubic cell. (b) Point cloud representation of the same cell, illustrating the distribution of integration nodes generated via the quasi-Monte Carlo method using Sobol sequences. The inner region is highlighted by a denser blue core.

piecewise constant function, equal to  $f_C$  in the inner cube and to a different constant  $f_E$  in the exterior matrix. Consequently,

$$\begin{aligned} [f]_{\mathbf{v}} &= \frac{1}{|\mathfrak{U}|} \int_{\mathfrak{U}} f(\mathbf{x}) e^{-i\mathbf{G}(\mathbf{v}) \cdot \mathbf{x}} d\mathbf{x} \\ &= \frac{1}{|\mathfrak{U}|} \left( f_E \int_E e^{-i\mathbf{G}(\mathbf{v}) \cdot \mathbf{x}} d\mathbf{x} + f_C \int_C e^{-i\mathbf{G}(\mathbf{v}) \cdot \mathbf{x}} d\mathbf{x} \right) \end{aligned} \quad (68)$$

and, since, the exterior matrix is such that

$$\int_E e^{-i\mathbf{G}(\mathbf{v}) \cdot \mathbf{x}} d\mathbf{x} = \int_{\mathfrak{U}} e^{-i\mathbf{G}(\mathbf{v}) \cdot \mathbf{x}} d\mathbf{x} - \int_C e^{-i\mathbf{G}(\mathbf{v}) \cdot \mathbf{x}} d\mathbf{x}, \quad (69)$$

the computation reduces to evaluating the integral over the whole cell and the integral over the inner cube. Taking this into account, and considering the regular lattice  $\frac{2\pi}{d}\mathbb{Z}^3$ , the integrals over the inner cube can be computed directly.

$$\int_C e^{-i\mathbf{G}(\mathbf{v}) \cdot \mathbf{x}} d\mathbf{x} = \frac{1}{d^3} I_{v_1} I_{v_2} I_{v_3}, \quad (70)$$

with

$$I_{v_i} = \begin{cases} \ell_C & \text{if } v_i = 0 \\ \frac{\ell_C d}{2\pi v_i} \left( e^{-i\frac{2\pi}{d} v_i \left( \frac{d}{2} + \frac{\ell_C}{2} \right)} - e^{-i\frac{2\pi}{d} v_i \left( \frac{d}{2} - \frac{\ell_C}{2} \right)} \right) & \text{otherwise.} \end{cases} \quad (71)$$

Therefore, since the analytic expression of the coefficients is available in this test case, the relative

error with respect to the quasi-Monte Carlo (qMC) approximation can be computed. Fig. 9 shows the relative error for the coefficients of  $\hat{C}_{1111}$ , where the qMC approximation is computed using  $N = 10^6$  points (left) and  $N = 10^8$  points (right). It is noted that the coefficients of the other tensor components and the mass density exhibit the same behavior, as only the constant values differ. As expected, increasing the number of points leads to a more accurate approximation of the coefficients. However, the approximation deteriorates as the multi-indices  $\mathbf{v}$  move away from the origin, due to the increasingly oscillatory behavior of the integrand.

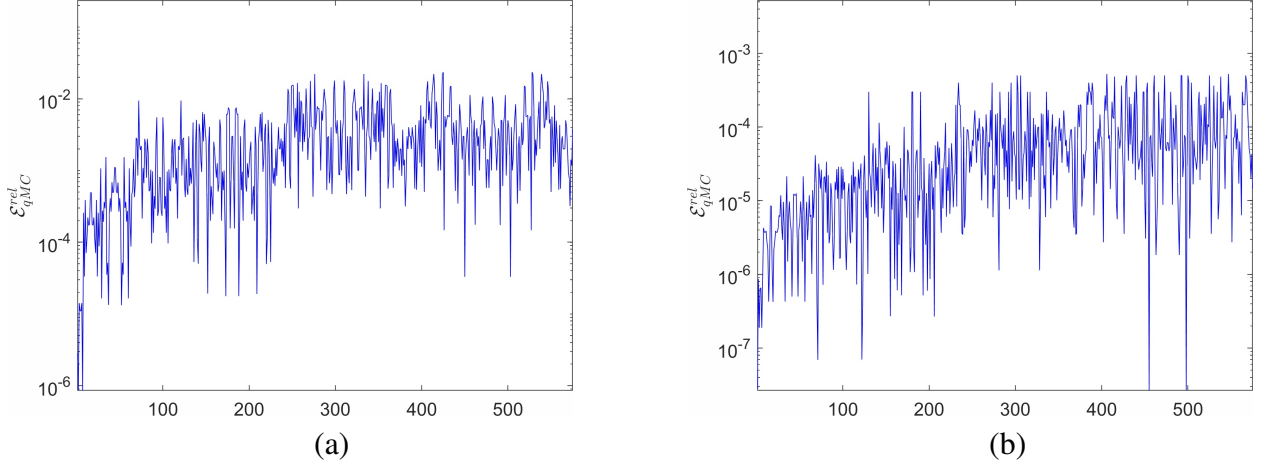


Figure 9: Relative error in the computation of the Fourier coefficients for all lattice indices satisfying  $\|\mathbf{v}\|_\infty \leq 7$ . (a) shows the result obtained with  $N = 10^6$  points, while (b) corresponds to  $N = 10^8$  points used in the quasi-Monte Carlo approximation.

## Appendix E: Fourier-based approach vs finite element model

The same geometry of the periodic cell described in Appendix D and schematically illustrated in Fig. 8 is considered here, with two idealized materials assigned to the inclusion and the surrounding matrix, respectively. The inclusion is made of a linear elastic isotropic material characterized by Young's modulus  $E = 10^4$  Pa, Poisson's ratio  $\nu = 0.3$ , and mass density  $\rho = 7500$  kg/m<sup>3</sup>. The matrix consists of a linear viscoelastic isotropic material, with mechanical properties  $E = 5 \cdot 10^3$  Pa,  $\nu = 0.3$ , and  $\rho = 1150$  kg/m<sup>3</sup>. Moreover, the components of the long-term relaxation tensor  $\mathbb{G}^\infty$  are expressed in terms of  $E$  and  $\nu$ , as detailed in Section 6. The infinite-dimensional algebraic eigenproblem, arising from the Fourier expansion-based scheme proposed here, has been truncated by retaining  $N$  harmonics. In particular, we considered the harmonics for which the lattice index  $\mathbf{v}$  is such that its infinity norm is smaller than 3. In addition, the qMC approximation of Fourier coefficients has been obtained by using  $10^6$  Sobol points. For a consistent one-to-one comparison, the long-term response constitutive tensor components  $G_{ijhk}^\infty$  used in the finite element model are approximated by Fourier polynomials with the same number of harmonics.

The Fig. 10 reports the results in terms of the Floquet spectrum and dispersion curves plotted on the unit cylindrical surface, represented through the real part of the normalized frequency, for two limiting cases of relaxation time:  $\tau_r \rightarrow 0$  (Fig.s (a) and (b)) and  $\tau_r \rightarrow \infty$  (Fig.s (c) and (d)). In both

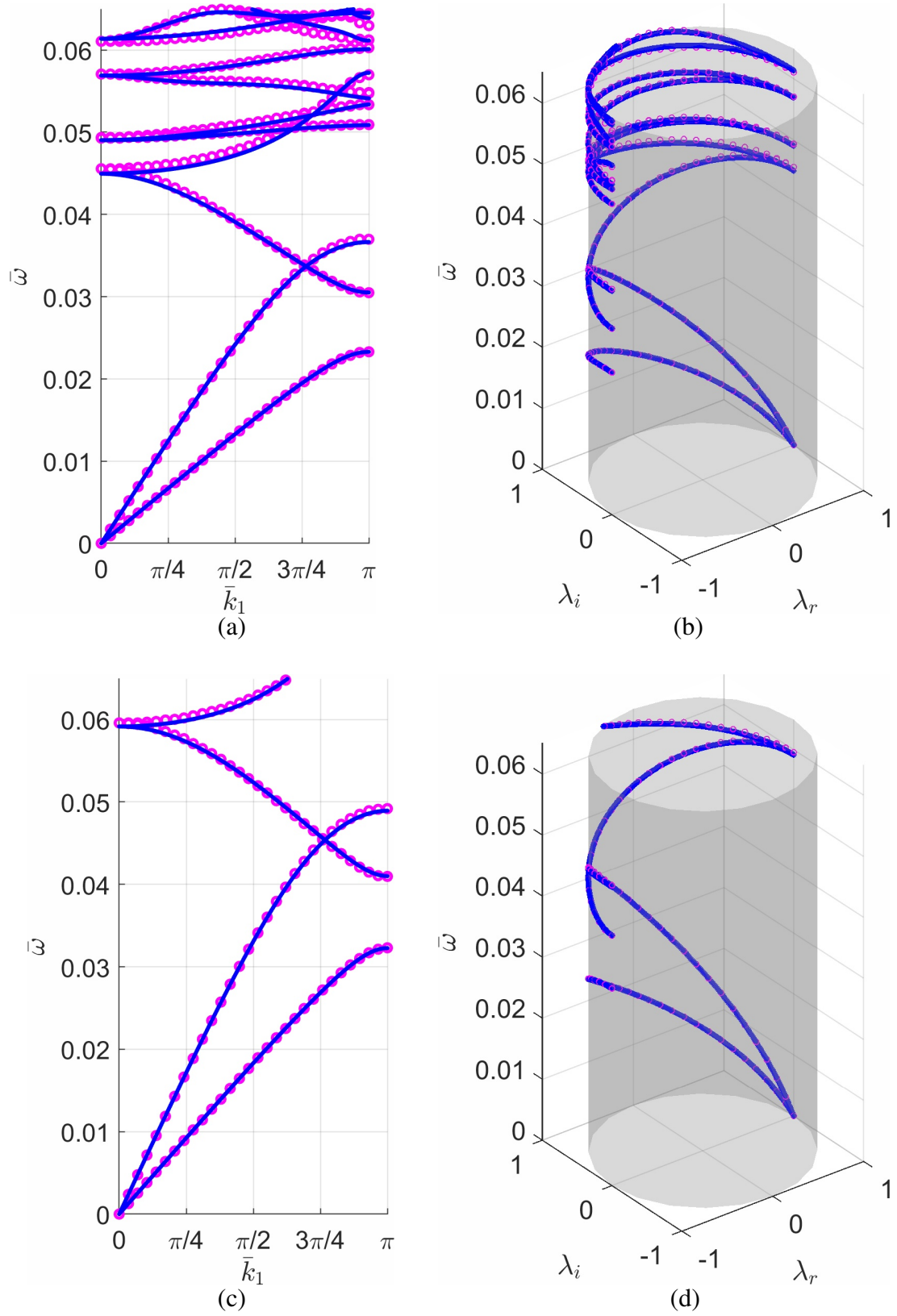


Figure 10:  $\bar{\omega} = \omega/\omega_{ref}$  vs  $\bar{k}_1 = k_1 d$  with  $\omega_{ref} = \frac{1}{d} \sqrt{\frac{E}{\rho}}$ , with  $E$  and  $\rho$  of the TMPS-layer (Fig.s (a) and (c)). Real and imaginary components of the Floquet multiplier  $\lambda = \exp(ik_1 d)$  vs  $\bar{\omega}$  (Fig.s (b) and (d)). Relaxation time  $\tau_r \rightarrow 0$  (Fig.s (a) and (b)) and  $\tau_r \rightarrow \infty$  (Fig.s (c) and (d)).

cases, the comparison with numerical results obtained from the finite element model implemented in the commercial software *COMSOL Multiphysics*<sup>®</sup> is highly satisfactory, confirming the ability of the proposed model to accurately capture the viscoelastic response of the material. As expected, since only propagating branches are considered, the curves in (b) and (d) wrap around the surface of the cylinders.

## References

- [1] Y.-F. Wang, Y.-S. Wang, and V. Laude. Wave propagation in two-dimensional viscoelastic metamaterials. *Physical Review B*, 92(10):104110, 2015.
- [2] A. Krushynska, V. Kouznetsova, and M. Geers. Visco-elastic effects on wave dispersion in three-phase acoustic metamaterials. *Journal of the Mechanics and Physics of Solids*, 96:29–47, 2016.
- [3] D. M. J. Dykstra, J. Busink, B. Ennis, and C. Coulais. Viscoelastic snapping metamaterials. *Journal of Applied Mechanics*, 86(11):111012, 09 2019.
- [4] V. Laude. *Phononic crystals: artificial crystals for sonic, acoustic, and elastic waves*. Walter de Gruyter GmbH & Co KG, 2020.
- [5] J. Zhang, B. Hu, and S. Wang. Review and perspective on acoustic metamaterials: From fundamentals to applications. *Applied Physics Letters*, 123(1), 2023.
- [6] W. J. Parnell and R. De Pascalis. Soft metamaterials with dynamic viscoelastic functionality tuned by pre-deformation. *Philosophical Transactions of the Royal Society A*, 377(2144):20180072, 2019.
- [7] D. Roca, D. Yago, J. Cante, O. Lloberas-Valls, and J. Oliver. Computational design of locally resonant acoustic metamaterials. *Computer Methods in Applied Mechanics and Engineering*, 345:161–182, 2019.
- [8] A. Bacigalupo, M. L. De Bellis, and D. Misseroni. Design of tunable acoustic metamaterials with periodic piezo-electric microstructure. *Extreme Mechanics Letters*, 40:100977, 2020.
- [9] M. Gei, Z. Chen, F. Bosi, and L. Morini. Phononic canonical quasicrystalline waveguides. *Applied Physics Letters*, 116(24), 2020.
- [10] R. Hu and C. Oskay. Spectral variational multiscale model for transient dynamics of phononic crystals and acoustic metamaterials. *Computer Methods in Applied Mechanics and Engineering*, 359:112761, 2020.
- [11] D. M. Dykstra, S. Janbaz, and C. Coulais. The extreme mechanics of viscoelastic metamaterials. *APL Materials*, 10(8), 2022.
- [12] S. Mora, N. M. Pugno, and D. Misseroni. 3d printed architected lattice structures by material jetting. *Materials Today*, 59:107–132, 2022.
- [13] M. Livani, A. S. Suiker, A. Crivellaro, and E. Bosco. A 3d multi-scale hygro-mechanical model of oak wood. *Wood Science and Technology*, 57(6):1215–1256, 2023.
- [14] S. Zang, D. Misseroni, T. Zhao, and G. H. Paulino. Kresling origami mechanics explained: Experiments and theory. *Journal of the Mechanics and Physics of Solids*, 188:105630, 2024.
- [15] R. Alberdi, C. Hamel, B. Talamini, and M. R. Tupek. An optimization-based approach to tailor the mechanical response of soft metamaterials undergoing rate-dependent instabilities. *Computer Methods in Applied Mechanics and Engineering*, 435:117679, 2025.
- [16] D. Roca, O. Lloberas-Valls, J. Cante, and J. Oliver. A computational multiscale homogenization framework accounting for inertial effects: Application to acoustic metamaterials modelling. *Computer methods in applied mechanics and engineering*, 330:415–446, 2018.
- [17] R. Del Toro, A. Bacigalupo, and M. Paggi. Characterization of wave propagation in periodic viscoelastic materials via asymptotic-variational homogenization. *International Journal of Solids and Structures*, 172-173:110–146, 2019.
- [18] P. A. Huidobro, M. G. Silveirinha, E. Galiffi, and J. Pendry. Homogenization theory of space-time metamaterials. *Physical Review Applied*, 16(1):014044, 2021.

- [19] E. Monaldo and S. Marfia. Computational homogenization of 3d printed materials by a reduced order model. *International Journal of Mechanical Sciences*, 197:106332, 2021.
- [20] A. Bacigalupo, M. L. De Bellis, and G. Zavarise. Asymptotic homogenization approach for anisotropic micropolar modeling of periodic cauchy materials. *Computer Methods in Applied Mechanics and Engineering*, 388:114201, 2022.
- [21] F. Fantoni and A. Bacigalupo. Multifield constitutive identification of non-conventional thermo-viscoelastic periodic cauchy materials. *International Journal of Mechanical Sciences*, 223:107228, 2022.
- [22] C. Mei, L. Li, X. Li, H. Tang, X. Han, X. Wang, and Y. Hu. A nonlocality-based homogenization method for dynamics of metamaterials. *Composite Structures*, 295:115716, 2022.
- [23] S. Li, W. Zheng, and L. Li. Spatiotemporally nonlocal homogenization method for viscoelastic porous metamaterial structures. *International Journal of Mechanical Sciences*, 282:109572, 2024.
- [24] J. Barceló-Mercader, D. Codony, A. Mocci, and I. Arias. Computational homogenization of higher-order electro-mechanical materials with built-in generalized periodicity conditions. *Computer Methods in Applied Mechanics and Engineering*, 423:116861, 2024.
- [25] R. Del Toro, M. L. De Bellis, M. Vasta, and A. Bacigalupo. Multifield asymptotic homogenization for periodic materials in non-standard thermoelasticity. *International Journal of Mechanical Sciences*, 265:108835, 2024.
- [26] I. V. Kamotski and V. P. Smyshlyaev. Bandgaps in two-dimensional high-contrast periodic elastic beam lattice materials. *Journal of the Mechanics and Physics of Solids*, 123:292–304, 2019.
- [27] M. Touboul, B. Vial, R. Assier, S. Guenneau, and R. V. Craster. High-frequency homogenization for periodic dispersive media. *Multiscale Modeling & Simulation*, 22(3):1136–1168, 2024.
- [28] R. Del Toro, M. L. De Bellis, and A. Bacigalupo. Dynamic continualization of mechanical metamaterials with quasi-periodic microstructure. *Philosophical Transactions A*, 382(2278):20230353, 2024.
- [29] R. Del Toro, M. L. De Bellis, and A. Bacigalupo. Design of a thermoelastic metafilter through non-local continualization methods. *International Journal of Mechanical Sciences*, 280:109483, 2024.
- [30] H. Goh and L. F. Kallivokas. Inverse band gap design of elastic metamaterials for p and sv wave control. *Computer Methods in Applied Mechanics and Engineering*, 370:113263, 2020.
- [31] A. Palermo and A. Marzani. A reduced bloch operator finite element method for fast calculation of elastic complex band structures. *International Journal of Solids and Structures*, 191:601–613, 2020.
- [32] S. van den Boom, F. van Keulen, and A. Aragón. Fully decoupling geometry from discretization in the bloch–floquet finite element analysis of phononic crystals. *Computer Methods in Applied Mechanics and Engineering*, 382:113848, 2021.
- [33] D. Préve, P. Lenarda, I. Maskery, and M. Paggi. A comprehensive characterization of fracture in unit cell open foams generated from triply periodic minimal surfaces. *Engineering Fracture Mechanics*, 277:108949, 2023.
- [34] M. Lewińska, V. Kouznetsova, J. Van Dommelen, A. Krushynska, and M. Geers. The attenuation performance of locally resonant acoustic metamaterials based on generalised viscoelastic modelling. *International Journal of Solids and Structures*, 126:163–174, 2017.
- [35] F. Vadalá, A. Bacigalupo, M. Lepidi, and L. Gambarotta. Free and forced wave propagation in beam lattice metamaterials with viscoelastic resonators. *International Journal of Mechanical Sciences*, 193:106129, 2021.
- [36] J.-M. Ricaud and R. Masson. Effective properties of linear viscoelastic heterogeneous media: Internal variables formulation and extension to ageing behaviours. *International Journal of Solids and Structures*, 46(7):1599–1606, 2009.
- [37] A. Arena, A. Bacigalupo, and M. Lepidi. Wave propagation in viscoelastic metamaterials via added-state formulation. *International Journal of Mechanical Sciences*, 228:107461, 2022.
- [38] V. Mehrmann and H. Voss. Nonlinear eigenvalue problems: a challenge for modern eigenvalue methods. *GAMM Mitt. Ges. Angew. Math. Mech.*, 27(2):121–152 (2005), 2004.
- [39] D. S. Mackey, N. Mackey, C. Mehl, and V. Mehrmann. Vector spaces of linearizations for matrix polynomials. *SIAM J. Matrix Anal. Appl.*, 28(4):971–1004, 2006.



- [40] D. S. Mackey, N. Mackey, C. Mehl, and V. Mehrmann. Structured polynomial eigenvalue problems: good vibrations from good linearizations. *SIAM J. Matrix Anal. Appl.*, 28(4):1029–1051, 2006.
- [41] A. Ruhe. Algorithms for the nonlinear eigenvalue problem. *SIAM J. Numer. Anal.*, 10:674–689, 1973.
- [42] P. Lietaert, K. Meerbergen, J. Pérez, and B. Vandereycken. Automatic rational approximation and linearization of nonlinear eigenvalue problems. *IMA J. Numer. Anal.*, 42(2):1087–1115, 2022.
- [43] G. Elefante, M. L. De Bellis, and A. Bacigalupo. Electrically-tunable active metamaterials for damped elastic wave propagation control. *Int. J. Solids Struct.*, 276:112306, 2023.
- [44] Y. Su and Z. Bai. Solving rational eigenvalue problems via linearization. *SIAM J. Matrix Anal. Appl.*, 32(1):201–216, 2011.
- [45] A. Bacigalupo, M. L. De Bellis, and G. Gnecco. Complex frequency band structure of periodic thermo-diffusive materials by Floquet–Bloch theory. *Acta Mechanica*, 230(9):3339–3363, 2019.
- [46] V. F. Dal Poggetto and A. L. Serpa. Elastic wave band gaps in a three-dimensional periodic metamaterial using the plane wave expansion method. *International Journal of Mechanical Sciences*, 184:105841, 2020.
- [47] P. Glasserman. *Monte Carlo methods in financial engineering*, volume 53 of *Applications of Mathematics (New York)*. Springer-Verlag, New York, 2004. Stochastic Modelling and Applied Probability.
- [48] S. H. Paskov and J. F. Traub. Faster valuation of financial derivatives. *J. Portf. Manag.*, 22(1):113–123, 1995.
- [49] C. Zhang, X. Wang, and Z. He. Efficient importance sampling in quasi-Monte Carlo methods for computational finance. *SIAM J. Sci. Comput.*, 43(1):B1–B29, 2021.
- [50] X. Wang, J. Li, and Z. Fang. Analysis and application of single level, multi-level Monte Carlo and quasi-Monte Carlo finite element methods for time-dependent Maxwell’s equations with random inputs. *Commun. Comput. Phys.*, 29(1):211–236, 2021.
- [51] A. Keller. Myths of computer graphics. In *Monte Carlo and quasi-Monte Carlo methods 2004*, pages 217–243. Springer, Berlin, 2006.
- [52] J. Dick and F. Pillichshammer. Discrepancy theory and quasi-monte carlo integration. In *A panorama of discrepancy theory*, pages 539–619. Springer, 2014.
- [53] H. Niederreiter. *Random number generation and quasi-Monte Carlo methods*, volume 63 of *CBMS-NSF Regional Conference Series in Applied Mathematics*. Society for Industrial and Applied Mathematics (SIAM), Philadelphia, PA, 1992.
- [54] J. Dick, F. Y. Kuo, and I. H. Sloan. High-dimensional integration: the quasi-Monte Carlo way. *Acta Numer.*, 22:133–288, 2013.
- [55] V. Gonsovskii and Y. A. Rossikhin. Stress waves in a viscoelastic medium with a singular hereditary kernel. *Journal of Applied Mechanics and Technical Physics*, 14(4):595–597, 1973.
- [56] M. Di Paola, A. Pirrotta, and A. Valenza. Visco-elastic behavior through fractional calculus: an easier method for best fitting experimental results. *Mechanics of materials*, 43(12):799–806, 2011.
- [57] P. Lenarda and M. Paggi. A computational framework for rheologically complex thermo-visco-elastic materials. *International Journal of Solids and Structures*, 236-237:111297, 2022.
- [58] J.-P. Berrut, S. De Marchi, G. Elefante, and F. Marchetti. Treating the Gibbs phenomenon in barycentric rational interpolation and approximation via the  $S$ -Gibbs algorithm. *Appl. Math. Lett.*, 103:106196, 7, 2020.
- [59] S. De Marchi, G. Elefante, and F. Marchetti. Stable discontinuous mapped bases: the Gibbs-Runge-avoiding stable polynomial approximation (GRASPA) method. *Comput. Appl. Math.*, 40(8):Paper No. 299, 17, 2021.
- [60] Y. Liu, Y. Li, J. Song, M. Luo, Z. He, C. Yang, J. Lv, D. Kong, J. Qiu, X. Hong, H. Guo, and J. Wu. Practical Kramers-Kronig phase retrieval FIR filter with the Gibbs phenomenon. *Journal of Lightwave Technology*, 40:1007–1017, 2022.
- [61] B. D. Shizgal and J.-H. Jung. Towards the resolution of the Gibbs phenomena. *J. Comput. Appl. Math.*, 161(1):41–65, 2003.
- [62] X. Yang, Y. Ding, J. Wang, G. Liu, and P. R. Palmer. An improved Fourier-series-based IGBT model by mitigating the effect of Gibbs phenomenon at turn on. *IEEE Transactions on Electron Devices*, 68:3453–3459, 2021.

- [63] A. J. Jerri. *The Gibbs phenomenon in Fourier analysis, splines and wavelet approximations*, volume 446. Springer Science & Business Media, 1998.
- [64] A. C. Antoulas. *Approximation of large-scale dynamical systems*, volume 6 of *Advances in Design and Control*. Society for Industrial and Applied Mathematics (SIAM), Philadelphia, PA, 2005.
- [65] H. Niederreiter. *Random number generation and quasi-Monte Carlo methods*, volume 63 of *CBMS-NSF Regional Conference Series in Applied Mathematics*. Society for Industrial and Applied Mathematics (SIAM), Philadelphia, PA, 1992.
- [66] W. Stute. Convergence rates for the isotrope discrepancy. *Ann. Probability*, 5(5):707–723, 1977.
- [67] L. Brandolini, L. Colzani, G. Gigante, and G. Travaglino. On the Koksma-Hlawka inequality. *J. Complexity*, 29(2):158–172, 2013.
- [68] S. De Marchi and G. Elefante. Quasi-Monte Carlo integration on manifolds with mapped low-discrepancy points and greedy minimal Riesz  $s$ -energy points. *Appl. Numer. Math.*, 127:110–124, 2018.
- [69] E. Artioli, G. Elefante, A. Sommariva, and M. Vianello. Homogenization of composite materials reinforced with unidirectional fibres with complex curvilinear cross section: a virtual element approach. *Math. Eng.*, 6(4):510–535, 2024.
- [70] G. Elefante, A. Sommariva, and M. Vianello. CQMC: an improved code for low-dimensional compressed quasi-Monte Carlo cubature. *Dolomites Res. Notes Approx.*, 15(2):92–100, 2022.
- [71] G. Elefante, A. Sommariva, and M. Vianello. Tchakaloff-like compression of QMC volume and surface integration on the union of balls. *Calcolo*, 61(3):Paper No. 46, 2024.
- [72] G. Elefante, A. Sommariva, and M. Vianello. Qsurf: compressed QMC integration on parametric surfaces. *Journal of Approximation Software*, 1(1), 2024.
- [73] T. Brunet, A. Merlin, B. Mascaro, K. Zimny, J. Leng, O. Poncelet, C. Aristégui, and O. Mondain-Monval. Soft 3d acoustic metamaterial with negative index. *Nature materials*, 14(4):384–388, 2015.
- [74] J. Pendry. A chiral route to negative refraction. *Science*, 306(5700):1353–1355, 2004.
- [75] X. Zheng, H. Lee, T. H. Weisgraber, M. Shusteff, J. DeOtte, E. B. Duoss, J. D. Kuntz, M. M. Biener, Q. Ge, J. A. Jackson, et al. Ultralight, ultrastiff mechanical metamaterials. *Science*, 344(6190):1373–1377, 2014.
- [76] F. Bobbert, K. Lietaert, A. A. Eftekhari, B. Pouran, S. Ahmadi, H. Weinans, and A. Zadpoor. Additively manufactured metallic porous biomaterials based on minimal surfaces: A unique combination of topological, mechanical, and mass transport properties. *Acta biomaterialia*, 53:572–584, 2017.
- [77] S. J. Callens, C. H. Arns, A. Kuliesh, and A. A. Zadpoor. Decoupling minimal surface metamaterial properties through multi-material hyperbolic tilings. *Advanced Functional Materials*, 31(30):2101373, 2021.
- [78] S. Hyde, Z. Blum, T. Landh, S. Lidin, B. Ninham, S. Andersson, and K. Larsson. *The language of shape: the role of curvature in condensed matter: physics, chemistry and biology*. Elsevier, 1996.
- [79] S. J. Callens, R. J. Uyttendaele, L. E. Fratila-Apachitei, and A. A. Zadpoor. Substrate curvature as a cue to guide spatiotemporal cell and tissue organization. *Biomaterials*, 232:119739, 2020.
- [80] R. Belda, R. Megías, M. Marco, A. Vercher-Martínez, and E. Giner. Numerical analysis of the influence of triply periodic minimal surface structures morphometry on the mechanical response. *Computer Methods and Programs in Biomedicine*, 230:107342, 2023.
- [81] C. Pouya, M. Kolle, J. Aizenberg, K. Bertoldi, J. C. Weaver, P. Vukusic, et al. Characterization of a mechanically tunable gyroid photonic crystal inspired by the butterfly parides sesostris. *Advanced Optical Materials*, 2015.
- [82] M. Lai, A. N. Kulak, D. Law, Z. Zhang, F. C. Meldrum, and D. J. Riley. Profiting from nature: macroporous copper with superior mechanical properties. *Chemical communications*, (34):3547–3549, 2007.
- [83] M. W. Matsen and F. S. Bates. Unifying weak-and strong-segregation block copolymer theories. *Macromolecules*, 29(4):1091–1098, 1996.
- [84] A. H. Schoen. *Infinite periodic minimal surfaces without self-intersections*, volume 5541. National Aeronautics and Space Administration, 1970.
- [85] H. J. Lee, S. Zhang, Y. Bar-Cohen, and S. Sherit. High temperature, high power piezoelectric composite transducers.

*Sensors*, 14(8):14526–14552, 2014.

- [86] J. M. Carcione. *Wave fields in real media: Wave propagation in anisotropic, anelastic, porous and electromagnetic media*. Elsevier, 2007.
- [87] F. Fantoni, A. Bacigalupo, G. Gnecco, and L. Gambarotta. Multi-objective optimal design of mechanical metafilters based on principal component analysis. *International Journal of Mechanical Sciences*, 248:108195, 2023.
- [88] J. Diani, P. Gilormini, C. Frédy, and I. Rousseau. Predicting thermal shape memory of crosslinked polymer networks from linear viscoelasticity. *International Journal of Solids and Structures*, 49(5):793–799, 2012.
- [89] A. R. Dusane, P. Lenarda, and M. Paggi. Computational modeling of viscoelastic backsheet materials for photovoltaics. *Mechanics of Materials*, 186:104810, 2023.
- [90] I. M. Sobol’. Distribution of points in a cube and approximate evaluation of integrals. *Ž. Vyčisl. Mat i Mat. Fiz.*, 7:784–802, 1967.